Frictionless line-to-line contact: Comparison of mortar and unbiased formulation in combination with Lagrange-multiplier and penalty method

Tomec, Jan; Jelenić, Gordan

International Journal of Solids and Structures 286-287 (2024) 112586

Contents lists available at ScienceDirect

International Journal of Solids and Structures

journal homepage: www.elsevier.com/locate/ijsolstr

Frictionless line-to-line contact: Comparison of mortar and unbiased formulation in combination with Lagrange-multiplier and penalty method ☆

Jan Tomec, Gordan Jelenić *

University of Rijeka, Faculty of Civil Engineering, Ul. Radmile Matejčić 3, 51000, Rijeka, Croatia

ARTICLE INFO

Keywords:
Line-to-line contact
Unbiased formulation
Mortar method
Penalty method
Lagrange multipliers

ABSTRACT

Recent developments in the beam-to-beam contact mechanics have prompted us to investigate further into the relations between different formulations and contact-force models. Specifically we address in this paper the recently developed mortar method for beams and develop its variant based on the penalty method. This allows an in-depth comparison between the two formulations. Furthermore, we design an unbiased approach and introduce a new discretisation technique developed specifically for this method. The unbiased line-to-line method is also combined both with the Lagrange-multiplier and the penalty method. All developed elements have been tested using the same examples to provide an objective comparison between formulations in terms of robustness and computational cost.

1. Introduction

For a variety of structural elements contact may be efficiently modelled using the mortar method (Belgacem et al., 1997; Belgacem, 1999; McDevitt and Laursen, 2000; Wohlmuth, 2001; Popp et al., 2009; Puso, 2004; Hüeber and Wohlmuth, 2005; Popp et al., 2010; Puso and Solberg, 2020), while for the beam-to-beam contact in general and even more so for the line-to-line, the penalty method is predominantly used (Durville, 2004; Chamekh et al., 2009; Durville, 2010; Meier et al., 2016, 2017). It has been argued that a beam as a semi-rigid body requires some artificially introduced flexibility of the cross-section to compensate for its rigidity in the mathematical model (Meier et al., 2016) causing discontinuities in the contact pressure. From Bosten et al. (2022) and Tomec and Jelenić (2022) we know, that Lagrange multipliers provide a reasonable alternative, resulting in fast and reliable convergence. This has previously been shown also on the point-to-point contact problems (Litewka, 2005).

The mortar method as implemented in Bosten et al. (2022) and Tomec and Jelenić (2022) is biased in the sense that the solution depends on the selection of the sides of the contact. Two-pass variant as tested in Tomec and Jelenić (2022) circumvents this problem and provides a robust formulation, but this requires two evaluations of the contact integral instead of one and is thus not optimal from the computational point of view. An alternative is to make the formulation itself unbiased, possibly opening space for better convergence path and improved robustness. Durville has achieved this in Durville (2010, 2012) by using average geometry, which is then used to define the normal vector and the gap function. The main drawback of this approach within the finite element method is that it requires identification of entire beams and contact zones so that the two sides have a meaningful average.

In this paper, we first summarise the mortar method as formalised in Tomec and Jelenić (2022) and present a penalty based collocation method akin to Gauss-point-to-segment method presented in Meier et al. (2016) in order to provide additional insight into comparative performance between the penalty and Lagrange-multiplier based line-to-line contact formulations. Then we propose a new approach on how to achieve an unbiased line-to-line formulation based on an unbiased parametrisation. Furthermore, we also develop its penalty variant to better illustrate the relation towards the other methods. All formulations result in contact elements, which are then rigorously tested using a range of numerical examples to elicit their characteristics related to bias, robustness, precision, convergence speed and computational burden.

All formulations to be described follow the same line of reasoning. First, the theory is developed for a continuous case starting with parametrisation of the contact, then the virtual work is computed and finally the linearisation is performed. Second, beam discretisation is introduced to define a contact element. Third, discrete residual vectors and tangent stiffness matrix contributions are provided.

☆ This work has received funding from the European Union's Horizon 2020 research and innovation programme under the Marie Skłodowska-Curie grant, Croatia agreement No 860124.

* Corresponding author.
E-mail addresses: jan.tomec@uniri.hr (J. Tomec), gordan.jelenic@uniri.hr (G. Jelenić).

https://doi.org/10.1016/j.ijsolstr.2023.112586
Received 20 February 2023; Received in revised form 13 November 2023; Accepted 15 November 2023
Available online 21 November 2023

2. Beam theory and discretisation

Beam is parametrised by a centreline $\mathbf{H} : \mathbb{R} \times [0, L] \subset \mathbb{R} \to SE(3); (t, s) \mapsto \mathbf{H}(t, s)$ to which a family of rigid cross-sections is attached. Configuration of the beam centreline can be separated into position $\boldsymbol{x} \in \mathbb{R}^3$ and rotation $\mathbf{R} \in SO(3)$. Presented contact formulations require only the knowledge about the position field.

According to the geometrically exact beam theory (Simo, 1985), beam's deformation can be measured using the following two strain vectors

$$\boldsymbol{\gamma} = \mathbf{R}^T \boldsymbol{x}' - \mathbf{R}_0^T \boldsymbol{x}_0', \tag{1}$$

$$\hat{\boldsymbol{\kappa}} = \mathbf{R}^T \mathbf{R}' - \mathbf{R}_0^T \mathbf{R}_0', \tag{2}$$

where $\hat{\cdot}$ maps a vector from a linear space to an appropriate Lie algebra ($\mathbb{R}^3 \mapsto \mathfrak{so}(3)$ and $\mathbb{R}^6 \mapsto \mathfrak{se}(3)$), $(\cdot)'$ denotes an arc-length derivative $\mathrm{d}/\mathrm{d}s$ and index 0 denotes a quantity in the undeformed configuration. Strains are related to internal forces via the material law

$$\boldsymbol{f}_{\text{int}} = \mathbf{K} \begin{Bmatrix} \boldsymbol{\gamma} \\ \boldsymbol{\kappa} \end{Bmatrix}. \tag{3}$$

We use a simple, linear-elastic material behaviour defining a diagonal stiffness matrix

$$\mathbf{K} = \operatorname{diag}\left(EA, GA_1, GA_2, GJ_t, EI_1, EI_2\right), \tag{4}$$

where E and G are material parameters called Young's and shear modulus, while the rest are geometric properties of the cross-section:

A	...	area,
A_1	...	area multiplied by the shear coefficient for the first principal axis,
A_2	...	area multiplied by the shear coefficient for the second principal axis,
J_t	...	torsional moment of inertia,
I_1	...	second moment of inertia around the first principal axis,
I_2	...	second moment of inertia around the second principal axis.

The spatial weak form of the static equilibrium equations from Simo and Vu-Quoc (1986) can be expressed using variations $\delta\mathbf{H} = \widehat{\delta\boldsymbol{h}}\mathbf{H}$. Using a six-dimensional vector representation, they can be combined into

$$\int_0^{L_0} \left(\delta\boldsymbol{h}^T \begin{bmatrix} \mathbf{0} & -\hat{\boldsymbol{x}}' \\ \mathbf{0} & \mathbf{0} \end{bmatrix} + \delta\boldsymbol{h}'^T \right) \boldsymbol{f}_{\text{int}} \mathrm{d}s - \int_0^{L_0} \delta\boldsymbol{h}^T \boldsymbol{f}_{\text{ext}} \mathrm{d}s = 0, \tag{5}$$

where L_0 is the initial length of the beam and $\boldsymbol{f}_{\text{ext}}$ are the external distributed forces along the beam.

In Simo and Vu-Quoc (1986), the authors use a separate interpolation of displacement and rotation. The rotation is updated directly in the integration points via interpolated incremental rotations. Elements of arbitrary order can be obtained by using the appropriate Lagrange interpolation polynomials.

Alternative discretisations of a beam are also possible (Bottasso and Borri, 1998; Crisfield and Jelenić, 1999; Ibrahimbegović, 1997; Hante et al., 2022; Sonneville et al., 2014, 2017; Zupan and Zupan, 2019). The presented contact formulations require continuously defined centreline position disqualifying formulations where the position is only known in the integration points (e.g. Bottasso and Borri, 1998 and Zupan and Zupan, 2019).

3. Contact between beams

Beam-to-beam contact takes place in two different ways based on the nature of the contact force. One is a line-to-line contact, where the force is distributed along the length of the actual contact zone. It describes well an interaction between parallel beams pressed against or twisted around each other. The second one is a point-to-point contact with the contact zone collapsing to a point. It happens when the beams touch at an angle. In this paper we discuss the line-to-line contact which can be viewed as the more general case capable to adequately describe as its specific case also point-to-point contact, as shown in our previous work (Tomec and Jelenić, 2022).

3.1. Contact constraints

Contact can be mathematically represented through the well-known Karush–Kuhn–Tucker (KKT) constraints (Popp et al., 2009). Using the Lagrange-multiplier field λ to represent the negative distributed contact pressure (distributed contact force along the beam) results in the following constraints:

$$g \geq 0 \tag{6a}$$

$$-\lambda \geq 0 \tag{6b}$$

$$\lambda g = 0 \tag{6c}$$

where g denotes the gap function. The gap is a geometrical measure of the distance between two beams (denoted as beam 1 and beam 2), which we want in a line-to-line method to be a continuous function, which serves to prevent penetration between the beams. It is defined as the distance between the two beam centrelines $\boldsymbol{x}_1(s_1)$ and $\boldsymbol{x}_2(s_2)$ reduced by the thicknesses of both beams

$$g = \|\boldsymbol{p}\| - \rho_1 - \rho_2, \tag{7}$$

where $\boldsymbol{p} = \boldsymbol{x}_1(s_1) - \boldsymbol{x}_2(s_2)$ and ρ_i is the cross-section radius of beam i. The geometry of the cross-section assumed in the contact formulation does not need to correspond exactly to the cross-section used in the beam theory. To relate the arc-length parameters s_i parametrising different centrelines, a projection map is used. This relation itself is the principal subject of this paper.

3.2. Contact potential and virtual work

Contribution of the frictionless contact to the total energy of the system can be defined by the contact potential as shown in Wriggers and Simo (1985)

$$\Pi_N = \int_{\Gamma_c} \lambda(s) g(s) \mathrm{d}s, \tag{8}$$

where Γ_c is the contact region and s is an arc-length parameter along the integration domain.

The virtual work arising from the contact potential is computed by varying this expression, obtaining

$$\delta\Pi_N = \int_{\Gamma_c} \delta\lambda g + \delta g \lambda \, \mathrm{d}s \tag{9}$$

where the explicit dependence of the fields λ and g on s has been omitted for clarity and the variation of the gap δg is yet to be determined. The gap function (7) is varied as

$$\begin{aligned} \delta g(s) &= \delta\sqrt{\boldsymbol{p}^T\boldsymbol{p}} \\ &= \delta\boldsymbol{p}^T \frac{\boldsymbol{p}}{\|\boldsymbol{p}\|} \\ &= \left(\delta\left[\boldsymbol{x}_1(s)\right] - \delta\left[\boldsymbol{x}_2(s)\right]\right)^T \boldsymbol{n} \\ &= \left(\delta\boldsymbol{x}_1 + \frac{\mathrm{d}\boldsymbol{x}_1}{\mathrm{d}s_1}\delta s_1 - \delta\boldsymbol{x}_2 - \frac{\mathrm{d}\boldsymbol{x}_2}{\mathrm{d}s_2}\delta s_2\right)^T \boldsymbol{n}, \end{aligned} \tag{10}$$

where $\boldsymbol{n} = \boldsymbol{p}/\|\boldsymbol{p}\|$ is the contact normal and $\delta\boldsymbol{x}_1$, $\delta\boldsymbol{x}_2$ are the variations of the centreline positions.

We can now express the contact virtual work as

$$\delta\Pi_N = \int_{\Gamma_c} \delta\lambda g + \left(\delta\boldsymbol{x}_1 - \delta\boldsymbol{x}_2\right)^T \boldsymbol{n}\lambda + \left(\boldsymbol{x}_1'\delta s_1 - \boldsymbol{x}_2'\delta s_2\right)^T \boldsymbol{n}\lambda \, \mathrm{d}s. \tag{11}$$

3.3. Mortar method

The mortar method is a discretisation method for contact between two, generally non-conforming, meshes. A mortar and a non-mortar side of the contact are assigned to allow simple parametrisation of the contact. A contact-force field is constructed using the existing domain discretisation on the non-mortar side. Here we present a summary of the method, while for further details the reader is referred to Tomec and Jelenić (2022).

Parametrisation

In the mortar method, the integration variable s simply corresponds to s_1 ($s = s_1$). The contact region Γ_c then reduces to the domain of beam 1, specifically, $s \in [0, L_1]$. This leads to the following development in the virtual work expression (11):

$$\delta\Pi_N = \int_0^{L_1} \delta\lambda g + \left(\delta\boldsymbol{x}_1 - \delta\boldsymbol{x}_2\right)^T \boldsymbol{n}\lambda - \delta s_2 \boldsymbol{x}_2'^T \boldsymbol{n}\lambda \,\mathrm{d}s_1, \tag{12}$$

because the parameter s_1 is fixed its variation δs_1 disappears.

Projection

In the mortar method, the orthogonal projection is used via

$$\boldsymbol{p}^T \boldsymbol{x}_2' = 0, \tag{13}$$

which implies $\boldsymbol{x}_2'^T \boldsymbol{n} = 0$ and thus the virtual work in (12) becomes

$$\delta\Pi_N = \int_0^{L_1} \delta\lambda g + \left(\delta\boldsymbol{x}_1 - \delta\boldsymbol{x}_2\right)^T \boldsymbol{n}\lambda \,\mathrm{d}s_1. \tag{14}$$

Note that δs_2 has disappeared from the expression, but it will come back with the linearisation. It is thus practical to derive it here and to explain its meaning, which follows from the interdependence between coordinates s_1 and s_2 based on the selected correlation equation — here the orthogonal projection (13). Because a contact relates two otherwise independent curves, its complete variation requires differentiation of both curves. The selected projection fixes the arc-length parameter on one side making it effectively independent of the other curve. The dependent side, however, does not experience the same simplification. Its complete variation thus also consists of differentiation with respect to the other curve.

Variation of (13)

$$\left(\delta\boldsymbol{x}_2' + \boldsymbol{x}_2''\delta s_2\right)^T \boldsymbol{p} + \left(\delta\boldsymbol{x}_1 - \delta\boldsymbol{x}_2 - \boldsymbol{x}_2'\delta s_2\right)^T \boldsymbol{x}_2' = 0$$

thus leads to

$$\delta s_2 = \frac{\left(\delta\boldsymbol{x}_1 - \delta\boldsymbol{x}_2\right)^T \boldsymbol{x}_2' + \delta\boldsymbol{x}_2'^T \boldsymbol{p}}{\boldsymbol{x}_2'^T \boldsymbol{x}_2' - \boldsymbol{p}^T \boldsymbol{x}_2''}. \tag{15}$$

Linearisation

To apply the Newton–Raphson algorithm, we now linearise the contact virtual work (14):

$$\begin{aligned}\Delta(\delta\Pi_N) = &\int_0^{L_1} \delta\lambda\Delta g \,\mathrm{d}s_1 + \int_0^{L_1} \left(\delta\boldsymbol{x}_1 - \delta\boldsymbol{x}_2\right)^T \boldsymbol{n}\Delta\lambda \,\mathrm{d}s_1 \\ &+ \int_0^{L_1} \left(\delta\boldsymbol{x}_1 - \delta\boldsymbol{x}_2\right)^T \Delta\boldsymbol{n}\lambda \,\mathrm{d}s_1 - \int_0^{L_1} \delta\boldsymbol{x}_2'^T \boldsymbol{n}\lambda\Delta s_2 \,\mathrm{d}s_1,\end{aligned} \tag{16}$$

where all of the terms are already known except for $\Delta\boldsymbol{n}$. It can be simply computed as

$$\begin{aligned}\Delta\boldsymbol{n} &= \Delta\left(\frac{\boldsymbol{p}}{\|\boldsymbol{p}\|}\right) \\ &= -\frac{\hat{\boldsymbol{n}}^2}{\|\boldsymbol{p}\|}\left(\Delta\left[\boldsymbol{x}_1(s_1)\right] - \Delta\left[\boldsymbol{x}_2(s_1)\right]\right) \\ &= -\frac{\hat{\boldsymbol{n}}^2}{\|\boldsymbol{p}\|}\left(\Delta\boldsymbol{x}_1 - \Delta\boldsymbol{x}_2 - \boldsymbol{x}_2'\Delta s_2\right),\end{aligned}$$

where $\hat{\cdot}$ maps to a skew symmetric matrix so that $\hat{\boldsymbol{a}}\boldsymbol{b} = \boldsymbol{a}\times\boldsymbol{b}$ for $\boldsymbol{a}, \boldsymbol{b} \in \mathbb{R}^3$. Because $\boldsymbol{n}^T\boldsymbol{x}_2' = 0$ and $\|\boldsymbol{n}\| = 1$, identity $\hat{\boldsymbol{n}}^2\boldsymbol{x}_2' = -\boldsymbol{x}_2'$ applies allowing the following development

$$\begin{aligned}\Delta\boldsymbol{n} &= -\frac{\hat{\boldsymbol{n}}^2}{\|\boldsymbol{p}\|}\left(\Delta\boldsymbol{x}_1 - \Delta\boldsymbol{x}_2\right) - \frac{1}{\|\boldsymbol{p}\|}\boldsymbol{x}_2'\Delta s_2 \\ &= -\frac{\hat{\boldsymbol{n}}^2}{\|\boldsymbol{p}\|}\left(\Delta\boldsymbol{x}_1 - \Delta\boldsymbol{x}_2\right) - \frac{1}{\|\boldsymbol{p}\|}\boldsymbol{x}_2'\frac{\boldsymbol{x}_2'^T\left(\Delta\boldsymbol{x}_1 - \Delta\boldsymbol{x}_2\right) + \boldsymbol{p}^T\Delta\boldsymbol{x}_2'}{\boldsymbol{x}_2'^T\boldsymbol{x}_2' - \boldsymbol{p}^T\boldsymbol{x}_2''} \\ &= -\frac{1}{\|\boldsymbol{p}\|}\left[\hat{\boldsymbol{n}}^2 + \frac{\boldsymbol{x}_2'\boldsymbol{x}_2'^T}{\boldsymbol{x}_2'^T\boldsymbol{x}_2' - \boldsymbol{p}^T\boldsymbol{x}_2''}\right]\left(\Delta\boldsymbol{x}_1 - \Delta\boldsymbol{x}_2\right) - \frac{\boldsymbol{x}_2'\boldsymbol{n}^T}{\boldsymbol{x}_2'^T\boldsymbol{x}_2' - \boldsymbol{p}^T\boldsymbol{x}_2''}\Delta\boldsymbol{x}_2'.\end{aligned} \tag{17}$$

By making use of the following substitutions

$$\mathbf{A} = \frac{1}{\|\boldsymbol{p}\|}\left[\hat{\boldsymbol{n}}^2 + \frac{\boldsymbol{x}_2'\boldsymbol{x}_2'^T}{\boldsymbol{x}_2'^T\boldsymbol{x}_2' - \boldsymbol{p}^T\boldsymbol{x}_2''}\right], \qquad \mathbf{B} = \frac{\boldsymbol{x}_2'\boldsymbol{n}^T}{\boldsymbol{x}_2'^T\boldsymbol{x}_2' - \boldsymbol{p}^T\boldsymbol{x}_2''}, \qquad \mathbf{C} = \frac{\boldsymbol{n}\boldsymbol{p}^T}{\boldsymbol{x}_2'^T\boldsymbol{x}_2' - \boldsymbol{p}^T\boldsymbol{x}_2''} \tag{18}$$

the linearised virtual work (16) can be written as

$$\begin{aligned}\Delta(\delta\Pi_N) = &\int_0^{L_1} \delta\lambda\boldsymbol{n}^T\left(\Delta\boldsymbol{x}_1 - \Delta\boldsymbol{x}_2\right) \mathrm{d}s_1 + \int_0^{L_1} \left(\delta\boldsymbol{x}_1 - \delta\boldsymbol{x}_2\right)^T \boldsymbol{n}\Delta\lambda \,\mathrm{d}s_1 \\ &- \int_0^{L_1} \left(\delta\boldsymbol{x}_1 - \delta\boldsymbol{x}_2\right)^T \lambda\left[\mathbf{A}\left(\Delta\boldsymbol{x}_1 - \Delta\boldsymbol{x}_2\right) + \mathbf{B}\Delta\boldsymbol{x}_2'\right] \mathrm{d}s_1 \\ &- \int_0^{L_1} \delta\boldsymbol{x}_2'^T\lambda\left[\mathbf{B}^T\left(\Delta\boldsymbol{x}_1 - \Delta\boldsymbol{x}_2\right) + \mathbf{C}\Delta\boldsymbol{x}_2'\right] \mathrm{d}s_1.\end{aligned} \tag{19}$$

Discretisation

A beam is discretised by dividing the entire domain into subdomains corresponding to the space of the arc-length parameter of an individual finite element. Since the virtual work (5) is defined through integration along the entire domain, splitting it directly corresponds to summation across all elements. Each element thus behaves as a continuous beam, but with its primary variables defined through interpolation of nodal values. Since this procedure is standard and known as the assembly of the finite elements, we will simplify the notation by skipping the reference to a particular element and re-use the notation from the continuum.

Although many different interpolations are possible, here we limit our attention only to a separate interpolation of the displacement and the rotation field. For a reference on how to transform the formulation to use the $SE(3)$ interpolation in combination with the material frame based residuals we refer the reader to Bosten et al. (2022). Polynomial-based interpolation of the position field can be found in many elements (Simo and Vu-Quoc, 1986; Ibrahimbegović, 1997; Crisfield and Jelenić, 1999). Let us define it and its variation for some element on beam i as

$$\boldsymbol{x}_i = \mathbf{N}_i^T\boldsymbol{X}_i, \qquad \delta\boldsymbol{x}_i = \mathbf{N}_i^T\delta\boldsymbol{X}_i, \tag{20}$$

where $\mathbf{N}_i$ is a matrix of shape functions

$$\mathbf{N}_i^T = \begin{bmatrix} N_{i1} & 0 & 0 & N_{i2} & 0 & 0 & \dots & N_{iM_{\mathrm{nodes},i}} & 0 & 0 \\ 0 & N_{i1} & 0 & 0 & N_{i2} & 0 & \dots & 0 & N_{iM_{\mathrm{nodes},i}} & 0 \\ 0 & 0 & N_{i1} & 0 & 0 & N_{i2} & \dots & 0 & 0 & N_{iM_{\mathrm{nodes},i}} \end{bmatrix}, \tag{21}$$

where $M_{\mathrm{nodes},i}$ is the number of nodes of an element on beam i and N_{ij} is a polynomial from Lagrange basis for node j of this element. The size of the matrix depends on the interpolation order. The vector $\boldsymbol{X}_i$ is the vector of nodal displacements of an element on beam i. Together with its variation $\delta\boldsymbol{X}_i$ they are both elements of $\mathbb{R}^{3M_{\mathrm{nodes},i}}$.

The discretisation of beams introduces discontinuities to the contact integral (12), which present a challenge for the numerical integration. The mortar method presented in Tomec and Jelenić (2022) addresses this issue by following the element-based integration (Farah et al.,

2015), where the contact integral subdomains correspond to the underlying non-mortar beam discretisation. To avoid further segmentation, such discretisation integrates across the discontinuities on the mortar side, effectively treating the beam as continuous. The same approach is used here as it has proved to be sufficient for the simple test cases. A simple Gaussian quadrature rule with fixed integration points is used for the numerical integration, where the number of points is defined as $2M_{\text{nodes},1}$, $M_{\text{nodes},1}$ being the number of nodes on the non-mortar side element. It should be noted, though, that this approach can lead to significant integration errors in certain cases. Disregarding the discretisation on the mortar side and integrating over weak discontinuities with a fixed number of integration points can lead to the kinks on the mortar side being close to the integration point, producing a relatively large error in the integral evaluation as noted in Farah et al. (2015) or even skipping entire mortar elements when the mesh on the mortar side is much finer than the one on the non-mortar side, leaving those elements uninvolved in the contact and the contact force unevenly distributed along the mortar side. These two issues are mainly not present in our cases as we mostly analyse similar meshes.

The third drawback of the adopted integration concerns the contact zone boundaries. Integrating over the boundary of the contact causes oscillations in the contact pressure when integrating over the boundary of the contact which represents a discontinuity in the Lagrange multipliers. A patch test with deformable bodies can thus not be passed (see Section 4.4), although the results are still mathematically meaningful. One way to remedy this is to implement boundary search and integrate based on the evaluated segments (Farah et al., 2015; Bosten et al., 2022). In our simple examples the oscillations do not seem to produce significant instabilities, which is why we decided not to deal with this issue and leave it for future improvements.

The Lagrange-multiplier field discretisation follows the discretisation of beam 1. This in principle means that each beam element on beam 1 has a corresponding contact element with its own interpolation of the Lagrange-multiplier field

$$\lambda = \boldsymbol{\Phi}^T \boldsymbol{\Lambda}, \qquad \delta\lambda = \boldsymbol{\Phi}^T \delta\boldsymbol{\Lambda}, \tag{22}$$

where $\boldsymbol{\Lambda} \in \mathbb{R}^{M_{\text{nodes},\Lambda}}$ is the vector of nodal Lagrange multipliers and

$$\boldsymbol{\Phi}^T = \left\{ \Phi_1 \quad \Phi_2 \quad \dots \quad \Phi_{M_{\text{nodes},\Lambda}} \right\}, \tag{23}$$

where $M_{\text{nodes},\Lambda}$ is the number of nodes of the contact element and Φ_j is a polynomial from Lagrange basis for node j of this element. Two interpolations are tested in numerical examples; one with a single node per element which results in a constant interpolation and one with two nodes per element, resulting in a C^0 continuous interpolation across the subdomains. The contact integration domain discretisation follows the non-mortar side beam discretisation. This ensures that each subdomain is continuously connected to its neighbours, optimally dividing the whole domain.

The discrete contact virtual work of an individual contact element is obtained by inserting the interpolated fields into (14)

$$\delta\Pi_N^{(el.)} = \delta\boldsymbol{\Lambda}^T \int_0^{L_1} \boldsymbol{\Phi} g \,\mathrm{d}s_1 + \delta\boldsymbol{X}_1^T \int_0^{L_1} \mathbf{N}_1 \boldsymbol{n} \lambda \,\mathrm{d}s_1 - \delta\boldsymbol{X}_2^T \int_0^{L_1} \mathbf{N}_2 \boldsymbol{n} \lambda \,\mathrm{d}s_1, \tag{24}$$

where L_1 and s_1 are the length and the coordinate of the corresponding beam 1 element. The whole domain is evaluated as the sum of all comprising elements

$$\delta\Pi_N = \sum_{(el.)} \delta\Pi_N^{(el.)}. \tag{25}$$

From (24) we can extract the residual vectors for individual contact element

$$\boldsymbol{R}_\lambda^{(el.)} = \int_0^{L_1} \boldsymbol{\Phi} g \,\mathrm{d}s_1, \qquad \boldsymbol{R}_1^{(el.)} = \int_0^{L_1} \mathbf{N}_1 \boldsymbol{n} \lambda \,\mathrm{d}s_1, \qquad \boldsymbol{R}_2^{(el.)} = -\int_0^{L_1} \mathbf{N}_2 \boldsymbol{n} \lambda \,\mathrm{d}s_1. \tag{26}$$

The linearised contact virtual work for an individual element (19) similarly becomes

$$\begin{aligned}
\Delta(\delta\Pi_N^{(el.)}) = {} & \delta\boldsymbol{\Lambda}^T \int_0^{L_1} \boldsymbol{\Phi}\boldsymbol{n}^T \mathbf{N}_1^T \,\mathrm{d}s_1 \,\Delta\boldsymbol{X}_1 - \delta\boldsymbol{\Lambda}^T \int_0^{L_1} \boldsymbol{\Phi}\boldsymbol{n}^T \mathbf{N}_2^T \,\mathrm{d}s_1 \,\Delta\boldsymbol{X}_2 \\
& + \delta\boldsymbol{X}_1^T \int_0^{L_1} \mathbf{N}_1 \boldsymbol{n}\boldsymbol{\Phi}^T \,\mathrm{d}s_1 \,\Delta\boldsymbol{\Lambda} - \delta\boldsymbol{X}_2^T \int_0^{L_1} \mathbf{N}_2 \boldsymbol{n}\boldsymbol{\Phi}^T \,\mathrm{d}s_1 \,\Delta\boldsymbol{\Lambda} \\
& - \delta\boldsymbol{X}_1^T \int_0^{L_1} \lambda \mathbf{N}_1 \mathbf{A} \mathbf{N}_1^T \,\mathrm{d}s_1 \,\Delta\boldsymbol{X}_1 \\
& + \delta\boldsymbol{X}_1^T \int_0^{L_1} \lambda \left[\mathbf{N}_1 \mathbf{A} \mathbf{N}_2^T - \mathbf{N}_1 \mathbf{B} \mathbf{N}_2'^T \right] \mathrm{d}s_1 \,\Delta\boldsymbol{X}_2 \\
& + \delta\boldsymbol{X}_2^T \int_0^{L_1} \lambda \left[\mathbf{N}_2 \mathbf{A} \mathbf{N}_1^T - \mathbf{N}_2 \mathbf{B}^T \mathbf{N}_1'^T \right] \mathrm{d}s_1 \,\Delta\boldsymbol{X}_1 \\
& - \delta\boldsymbol{X}_2^T \int_0^{L_1} \lambda \left[\mathbf{N}_2 \mathbf{A} \mathbf{N}_2^T - \mathbf{N}_2 \mathbf{B} \mathbf{N}_2'^T - \mathbf{N}_2' \mathbf{B}^T \mathbf{N}_2^T + \mathbf{N}_2' \mathbf{C} \mathbf{N}_2'^T \right] \mathrm{d}s_1 \,\Delta\boldsymbol{X}_2
\end{aligned} \tag{27}$$

from where we can extract the tangent stiffness matrices

$$\begin{aligned}
\mathbf{K}_{\lambda 1}^{(el.)} = \left(\mathbf{K}_{1\lambda}^{(el.)} \right)^T = \int_0^{L_1} \boldsymbol{\Phi}\boldsymbol{n}^T \mathbf{N}_1^T \,\mathrm{d}s_1, \qquad \mathbf{K}_{\lambda 2}^{(el.)} = \left(\mathbf{K}_{2\lambda}^{(el.)} \right)^T = -\int_0^{L_1} \boldsymbol{\Phi}\boldsymbol{n}^T \mathbf{N}_2^T \,\mathrm{d}s_1, \\
\mathbf{K}_{11}^{(el.)} = -\int_0^{L_1} \lambda \mathbf{N}_1 \mathbf{A} \mathbf{N}_1^T \,\mathrm{d}s_1, \\
\mathbf{K}_{12}^{(el.)} = \int_0^{L_1} \lambda \mathbf{N}_1 \left[\mathbf{A} \mathbf{N}_2^T - \mathbf{B} \mathbf{N}_2'^T \right] \mathrm{d}s_1, \\
\mathbf{K}_{21}^{(el.)} = \int_0^{L_1} \lambda \mathbf{N}_2 \left[\mathbf{A} \mathbf{N}_1^T - \mathbf{B}^T \mathbf{N}_1'^T \right] \mathrm{d}s_1, \\
\mathbf{K}_{22}^{(el.)} = -\int_0^{L_1} \lambda \left[\mathbf{N}_2 \mathbf{A} \mathbf{N}_2^T - \mathbf{N}_2 \mathbf{B} \mathbf{N}_2'^T - \mathbf{N}_2' \mathbf{B}^T \mathbf{N}_2^T + \mathbf{N}_2' \mathbf{C} \mathbf{N}_2'^T \right] \mathrm{d}s_1.
\end{aligned} \tag{28}$$

A contact involves three different sets of the nodal degrees of freedom: two sets for each beam element and one set for the Lagrange multipliers. This is reflected in the subscripts of the residual vectors and stiffness matrices. For example, $\boldsymbol{R}_\lambda^{(el.)}$ refers to the vector of residual forces at the Lagrange multiplier nodes, while $\mathbf{K}_{21}^{(el.)}$ refers to the tangent stiffness matrix that is obtained when we linearise the residual vector of the second beam element with respect to the degrees of freedom of the first element.

Penalty method

Within the mathematical model, Lagrange multipliers provide the optimal way to enforce contact constraints. However, in some cases it is beneficiary to use a less strict enforcement of contact condition using the penalty method.

The mortar method may be adapted for use with a penalty approach in which case the contact pressure is defined as

$$\lambda = \varepsilon g \tag{29}$$

$$\varepsilon = \begin{cases} \varepsilon_0, & \text{if } g < 0 \\ 0 & \text{otherwise} \end{cases} \tag{30}$$

where ε_0 is the penalty parameter. The contact potential (8) is multiplied with 1/2 to simplify later expressions for the residual forces and thus becomes

$$\Pi_N = \frac{1}{2} \int_{\Gamma_c} \lambda g \mathrm{d}s = \frac{1}{2} \int_{\Gamma_c} \varepsilon g^2 \mathrm{d}s. \tag{31}$$

Using the discretisation from the previous section, the contact-element residuals (26) eventually turn into

$$\boldsymbol{R}_1^{(el.)} = \int_0^{L_1} \varepsilon g \mathbf{N}_1 \boldsymbol{n} \,\mathrm{d}s_1, \qquad \boldsymbol{R}_2^{(el.)} = -\int_0^{L_1} \varepsilon g \mathbf{N}_2 \boldsymbol{n} \,\mathrm{d}s_1, \tag{32}$$

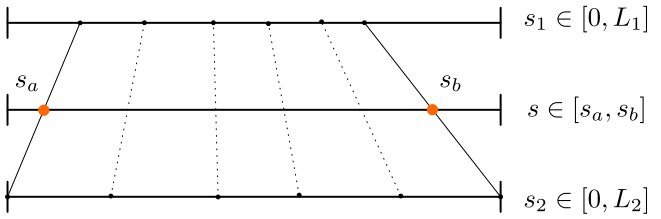

Fig. 1. Illustration of the integration parameter s in a continuum. Connecting lines show the projection (35) from parameter space s_2 to s_1 and, since the projection is one-to-one, vice versa. In the middle, the integration parameter s is illustrated as the average of s_1 and s_2.

while the contact-element tangent stiffness matrices (28) turn into

$$\begin{aligned}
\mathbf{K}_{11}^{(el.)} &= -\int_0^{L_1} \varepsilon g \mathbf{N}_1 \mathbf{A} \mathbf{N}_1^T - \varepsilon \mathbf{N}_1 \boldsymbol{n}\boldsymbol{n}^T \mathbf{N}_1^T \,\mathrm{d}s_1,\\
\mathbf{K}_{12}^{(el.)} &= \int_0^{L_1} \varepsilon g \mathbf{N}_1 \left[\mathbf{A} \mathbf{N}_2^T - \mathbf{B} \mathbf{N}_2'^T\right] - \varepsilon \mathbf{N}_1 \boldsymbol{n}\boldsymbol{n}^T \mathbf{N}_2^T \,\mathrm{d}s_1,\\
\mathbf{K}_{21}^{(el.)} &= \int_0^{L_1} \varepsilon g \mathbf{N}_2 \left[\mathbf{A} \mathbf{N}_1^T - \mathbf{B}^T \mathbf{N}_1'^T\right] - \varepsilon \mathbf{N}_2 \boldsymbol{n}\boldsymbol{n}^T \mathbf{N}_1^T \,\mathrm{d}s_1,\\
\mathbf{K}_{22}^{(el.)} &= -\int_0^{L_1} \varepsilon g \left[\mathbf{N}_2 \mathbf{A} \mathbf{N}_2^T - \mathbf{N}_2 \mathbf{B} \mathbf{N}_2'^T - \mathbf{N}_2' \mathbf{B}^T \mathbf{N}_2^T + \mathbf{N}_2' \mathbf{C} \mathbf{N}_2'^T\right] - \varepsilon \mathbf{N}_2 \boldsymbol{n}\boldsymbol{n}^T \mathbf{N}_2^T \,\mathrm{d}s_1.
\end{aligned} \tag{33}$$

Remark 1. Elimination of the Lagrange-multiplier field transforms the mortar method using a weak enforcement of the contact conditions to a collocation method with a strong enforcement of the contact conditions at the integration points. The algorithm becomes similar to the Gauss-point-to-segment method developed by Chamekh et al. (2009) and Meier et al. (2016). This form of penalisation is susceptible to locking at high values of the penalty parameter leading to oscillations, as shown in example 4.3.

3.4. Unbiased line-to-line method

Now we present our new formulation developed to provide an unbiased distributed contact element, which does not discriminate between the two sides of the contact. This is achieved by coupling the beam elements prone to contact, where each pair of elements defines a particular contact element.

Parametrisation and projection

The design goal of the unbiased line-to-line contact formulation is to obtain reliable and unique results regardless of the choice of curves 1 and 2, which must be reflected also in the discretised form within the finite element method. For this purpose we propose the following definition of the parametric variable s (illustrated in Fig. 1)

$$s = \frac{s_1 + s_2}{2} \tag{34}$$

with $s_i \in [0, L_i]$ for $i = 1, 2$ (where L_i is the undeformed arc-length of the centreline i), in combination with an appropriate projection function

$$\boldsymbol{p}^T \boldsymbol{t} = 0, \quad \boldsymbol{t} = \boldsymbol{x}_1' + \boldsymbol{x}_2'. \tag{35}$$

Parameters s_1 and s_2 are then computed by solving (34) and (35) using the Newton–Raphson method as explained in Appendix.

Eqs. (34) and (35) are not only symmetric, thus providing the required indifference of the solution to the curve selection, but also provide a similar simplified virtual contact work as in the mortar method (14) as will be shown later in the section. The integration domain must contain the entire contact zone, i.e. the entire subdomain where $g(s) < 0$ must be included. Therefore, the integration boundaries must be accurately obtained. They are computed through projections, summarised in the following algorithm

Box 1: Determining integration boundaries

1. Compute projections at boundaries $s_2(s_1 = 0)$, $s_1(s_2 = 0)$, $s_2(s_1 = L_1)$ and $s_1(s_2 = L_2)$*. Store each projection as a pair of beam arc-length parameters $c_k = (s_{1k}, s_{2k})$.
   * *Although a projection is straightforward to compute using the algorithm explained in Appendix, the correct solution is a global minimum which is not always the one that is obtained, depending on the initial value for the Newton–Raphson method.*
2. Either none or two of these projections can fall within the domain $s_{ik} \in [0, L_i]$ for $i = 1, 2$. Numerical errors might cause a different number of projections to be within the domain, too. If there is only one projection within the domain, another one, that is the closest to it, is added (if $s_{ik} \notin [0, L_i]$, then choose projection c_k so that $\min_k(|L_i/2 - s_{ik}|)$). Otherwise proceed.
3. If there are no projections within the domain $s_{ik} \in [0, L_i]$ for $i = 1, 2$, the possibility of contact between the two beams is disregarded. Otherwise, the integration domain is computed considering all valid projections as follows. The contact domain parameter s is first computed as $s_k = (s_{1k} + s_{2k})/2$. To handle different beam parametrisations, $\bar{s}_k = (s_{1k} - s_{2k})/2$ is also considered. The distance tensor is next constructed by computing $d_{kl} = |s_k - s_l|$ and $\bar{d}_{kl} = |\bar{s}_k - \bar{s}_l|$ for k and l going through all projections. The longest integration domain is then selected by finding the maximum value of the two distance tensors. Furthermore, if the maximum value is in $\bar{d}_{kl}$, parametrisation of one beam must be inverted.
4. Finally, the integration boundaries are chosen to correspond to the selected maximum value of the distance tensors. Additionally, the resulting integration domain must be longer then a certain threshold to be considered. After some testing we have set the threshold to be $0.1(L_1 + L_2)$. This eliminates very small elements.

With the integration boundaries determined, we can proceed with the derivation of the virtual work. Since s is fixed, variation of (34) reduces to

$$\delta s_1 = -\delta s_2 \tag{36}$$

and the variation of the gap function (10) becomes

$$\begin{aligned}
\delta g(s) &= \left(\delta \boldsymbol{x}_1 - \delta \boldsymbol{x}_2 + \frac{\mathrm{d}\boldsymbol{x}_1}{\mathrm{d}s_1}\delta s_1 + \frac{\mathrm{d}\boldsymbol{x}_2}{\mathrm{d}s_2}\delta s_1\right)^T \boldsymbol{n}\\
&= \left(\delta \boldsymbol{x}_1 - \delta \boldsymbol{x}_2\right)^T \boldsymbol{n}.
\end{aligned} \tag{37}$$

The virtual contact work follows from (11), however, since the integration limits s_a and s_b are variable, the Leibniz integral rule applies leading to

$$\begin{aligned}
\delta \Pi_N &= g(s_b)\lambda(s_b)\delta s_b - g(s_a)\lambda(s_a)\delta s_a\\
&\quad + \int_{s_a}^{s_b} \delta\lambda g + \left(\delta \boldsymbol{x}_1 - \delta \boldsymbol{x}_2\right)^T \boldsymbol{n}\lambda + \delta s_1 \left(\boldsymbol{x}_1' + \boldsymbol{x}_2'\right)^T \boldsymbol{n}\lambda \,\mathrm{d}s
\end{aligned} \tag{38}$$

and because of the zero-work constraint (6c) and the projection (35) it reduces to

$$\delta \Pi_N = \int_{s_a}^{s_b} \delta\lambda g + \left(\delta \boldsymbol{x}_1 - \delta \boldsymbol{x}_2\right)^T \boldsymbol{n}\lambda \,\mathrm{d}s. \tag{39}$$

The variation of projection function (35) reads

$$\begin{aligned}
&\left(\delta\left[\boldsymbol{x}_1(s)\right] - \delta\left[\boldsymbol{x}_2(s)\right]\right)^T \boldsymbol{t} + \left(\delta\left[\boldsymbol{x}_1'(s)\right] + \delta\left[\boldsymbol{x}_2'(s)\right]\right)^T \boldsymbol{p} = 0\\
&\left(\delta \boldsymbol{x}_1 - \delta \boldsymbol{x}_2 + \boldsymbol{x}_1' \delta s_1 - \boldsymbol{x}_2' \delta s_2\right)^T \boldsymbol{t} + \left(\delta \boldsymbol{x}_1' + \delta \boldsymbol{x}_2' + \boldsymbol{x}_1'' \delta s_1 + \boldsymbol{x}_2'' \delta s_2\right)^T \boldsymbol{p} = 0,
\end{aligned}$$

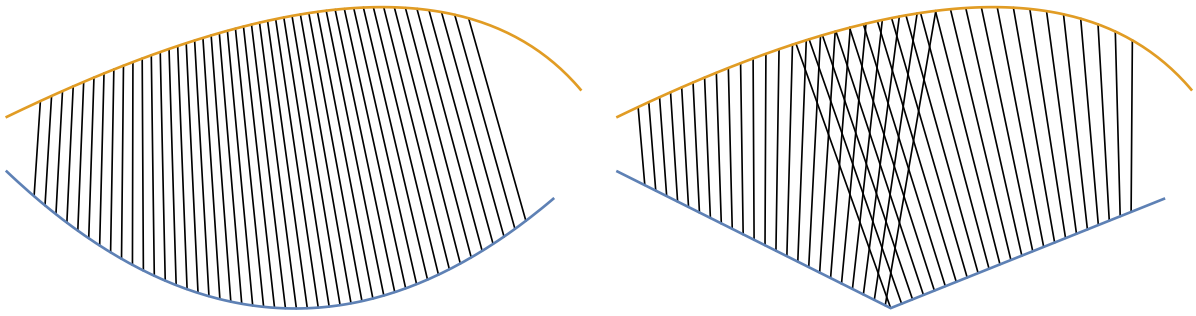

(a) Continuous contact formulation (b) Discretised contact

Fig. 2. Projection vectors between two beams.

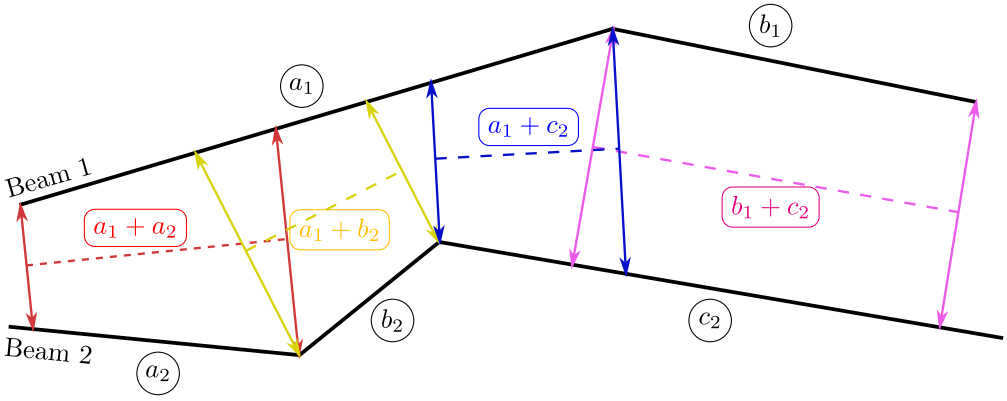

Fig. 3. Example of contact discretisation with unbiased line-to-line elements.

which after substituting (36) yields

$$\delta s_2 = \frac{\left(\delta \boldsymbol{x}_1 - \delta \boldsymbol{x}_2\right)^T \boldsymbol{t} + \left(\delta \boldsymbol{x}_1' + \delta \boldsymbol{x}_2'\right)^T \boldsymbol{p}}{\boldsymbol{t}^T \boldsymbol{t} + \left(\boldsymbol{x}_1'' - \boldsymbol{x}_2''\right)^T \boldsymbol{p}}. \tag{40}$$

Linearisation

The linearisation is performed as in the mortar method with the variation of projection function now being different. Linearised virtual work (39) is

$$\begin{aligned}\Delta(\delta \Pi_N) = &\int_{s_a}^{s_b} \delta\lambda \Delta g \,\mathrm{d}s + \int_{s_a}^{s_b} \left(\delta \boldsymbol{x}_1 - \delta \boldsymbol{x}_2\right)^T \boldsymbol{n} \Delta\lambda \,\mathrm{d}s \\ &+ \int_{s_a}^{s_b} \left(\delta \boldsymbol{x}_1 - \delta \boldsymbol{x}_2\right)^T \Delta\boldsymbol{n} \lambda \,\mathrm{d}s - \int_{s_a}^{s_b} \left(\delta \boldsymbol{x}_1' + \delta \boldsymbol{x}_2'\right)^T \boldsymbol{n} \lambda \Delta s_2 \,\mathrm{d}s.\end{aligned} \tag{41}$$

Extra terms due to the Leibniz integration rule for variable integration boundaries are neglected because the algorithm to determine the boundaries is non-differentiable (non-smooth switches between projection $s_1(s_2 = 0)$ and $s_2(s_1 = 0)$ or $s_1(s_2 = L_2)$ and $s_2(s_1 = L_1)$, see Box 1). The normal vector is linearised in a similar way to (17), eventually leading to

$$\begin{aligned}\Delta\boldsymbol{n} &= -\frac{\hat{\boldsymbol{n}}^2}{\|\boldsymbol{p}\|}\left(\Delta\left[\boldsymbol{x}_1(s)\right] - \Delta\left[\boldsymbol{x}_2(s)\right]\right) \\ &= -\frac{\hat{\boldsymbol{n}}^2}{\|\boldsymbol{p}\|}\left(\Delta\boldsymbol{x}_1 - \Delta\boldsymbol{x}_2 + \boldsymbol{x}_1' \Delta s_1 - \boldsymbol{x}_2' \Delta s_2\right) \\ &= -\frac{\hat{\boldsymbol{n}}^2}{\|\boldsymbol{p}\|}\left(\Delta\boldsymbol{x}_1 - \Delta\boldsymbol{x}_2 - \left(\boldsymbol{x}_1' + \boldsymbol{x}_2'\right)\Delta s_2\right)\end{aligned}$$

and using the $\hat{\boldsymbol{n}}^2\left(\boldsymbol{x}_1' + \boldsymbol{x}_2'\right) = -\boldsymbol{t}$ as in (17) we get

$$\begin{aligned}\Delta\boldsymbol{n} &= -\frac{\hat{\boldsymbol{n}}^2}{\|\boldsymbol{p}\|}\left(\Delta\boldsymbol{x}_1 - \Delta\boldsymbol{x}_2\right) - \frac{1}{\|\boldsymbol{p}\|}\boldsymbol{t}\Delta s_2 \\ &= -\frac{\hat{\boldsymbol{n}}^2}{\|\boldsymbol{p}\|}\left(\Delta\boldsymbol{x}_1 - \Delta\boldsymbol{x}_2\right) - \frac{1}{\|\boldsymbol{p}\|}\boldsymbol{t}\frac{\boldsymbol{t}^T\left(\Delta\boldsymbol{x}_1 - \Delta\boldsymbol{x}_2\right) + \boldsymbol{p}^T\left(\Delta\boldsymbol{x}_1' + \Delta\boldsymbol{x}_2'\right)}{\boldsymbol{t}^T\boldsymbol{t} + \left(\boldsymbol{x}_1'' - \boldsymbol{x}_2''\right)^T\boldsymbol{p}} \\ &= -\frac{1}{\|\boldsymbol{p}\|}\left[\hat{\boldsymbol{n}}^2 + \frac{\boldsymbol{t}\boldsymbol{t}^T}{\boldsymbol{t}^T\boldsymbol{t} + \left(\boldsymbol{x}_1'' - \boldsymbol{x}_2''\right)^T\boldsymbol{p}}\right]\left(\Delta\boldsymbol{x}_1 - \Delta\boldsymbol{x}_2\right) \\ &\quad - \frac{\boldsymbol{t}\boldsymbol{n}^T}{\boldsymbol{t}^T\boldsymbol{t} + \left(\boldsymbol{x}_1'' - \boldsymbol{x}_2''\right)^T\boldsymbol{p}}\left(\Delta\boldsymbol{x}_1' + \Delta\boldsymbol{x}_2'\right)\end{aligned} \tag{42}$$

from where we can similarly to (18) recognise the following three matrices

$$\begin{aligned}\mathbf{A} &= \frac{1}{\|\boldsymbol{p}\|}\left[\hat{\boldsymbol{n}}^2 + \frac{\boldsymbol{t}\boldsymbol{t}^T}{\boldsymbol{t}^T\boldsymbol{t} + \left(\boldsymbol{x}_1'' - \boldsymbol{x}_2''\right)^T\boldsymbol{p}}\right], \\ \mathbf{B} &= \frac{\boldsymbol{t}\boldsymbol{n}^T}{\boldsymbol{t}^T\boldsymbol{t} + \left(\boldsymbol{x}_1'' - \boldsymbol{x}_2''\right)^T\boldsymbol{p}}, \qquad \mathbf{C} = \frac{\boldsymbol{n}\boldsymbol{p}^T}{\boldsymbol{t}^T\boldsymbol{t} + \left(\boldsymbol{x}_1'' - \boldsymbol{x}_2''\right)^T\boldsymbol{p}}.\end{aligned} \tag{43}$$

We can insert the results directly into (41) to obtain

$$\begin{aligned}\Delta(\delta \Pi_N) = &\int_{s_a}^{s_b} \delta\lambda \boldsymbol{n}^T\left(\Delta\boldsymbol{x}_1 - \Delta\boldsymbol{x}_2\right) \mathrm{d}s + \int_{s_a}^{s_b} \left(\delta \boldsymbol{x}_1 - \delta \boldsymbol{x}_2\right)^T \boldsymbol{n} \Delta\lambda \,\mathrm{d}s \\ &- \int_{s_a}^{s_b} \left(\delta \boldsymbol{x}_1 - \delta \boldsymbol{x}_2\right)^T \lambda\left[\mathbf{A}\left(\Delta\boldsymbol{x}_1 - \Delta\boldsymbol{x}_2\right) + \mathbf{B}\left(\Delta\boldsymbol{x}_1' + \Delta\boldsymbol{x}_2'\right)\right] \mathrm{d}s \\ &- \int_{s_a}^{s_b} \left(\delta \boldsymbol{x}_1' + \delta \boldsymbol{x}_2'\right)^T \lambda\left[\mathbf{B}^T\left(\Delta\boldsymbol{x}_1 - \Delta\boldsymbol{x}_2\right) + \mathbf{C}\left(\Delta\boldsymbol{x}_1' + \Delta\boldsymbol{x}_2'\right)\right] \mathrm{d}s.\end{aligned} \tag{44}$$

Discretisation

Beam discretisation is already defined in (20) and (21). Accordingly, the contact integral (39) must be divided into subdomains to allow numerical integration. The integral is defined using the integration parameter s which depends on the arc-length parameters of the beams. This forces us to use segment-based integration which, on the positive side, avoids integrating over discontinuities but suffers from increased computational cost (Farah et al., 2015). Each segment defines a contact element. The segments are constructed by coupling the beam elements that are prone to contact and evaluating their individual contact zone using the algorithm in Box 1.

Unfortunantely, the discretised centrelines are only C^0 continuous so the contact segments are not necessarily continuously defined along the contact, see Figs. 2 and 3. This means that the discretised Lagrange-multiplier field must be defined individually per element and cannot be connected with neighbouring elements, resulting in a non-conforming Lagrange-multiplier field. Compared to the standard mortar method, this leads to an increased number of Lagrange multipliers' degrees of freedom and possible over-constraining, which can be avoided using the constant Lagrange multipliers' field interpolation. Since beams are often interpolated with higher order polynomials, the whole affair could also be remedied using $C^{(1)}$ continuous interpolation of displacement, e.g. Litewka (2007), as it would result in a continuous contact zone in the discretised setting. This would result in a framework where contact elements have a smooth transition between them and would furthermore allow $C^{(0)}$ continuous discretisation of the Lagrange multiplier field. However, this is left for future research.

As a result, each unbiased contact element couples a pair of beam elements with independent Lagrange multiplier nodes. This is in contrast to the mortar method where a contact element couples a single non-mortar-side beam element to potentially multiple mortar-side beam elements.

The contact element is, despite different discretisation, almost the same as in the mortar method. The Lagrange-multiplier field is interpolated as in (22), the nodes however now being specific to each element and not shared by the neighbouring elements. The resulting residual vectors and tangent matrices are also similar to (26) and (28). The discrete virtual work is obtained by inserting (20) and (22) into (39) and reads

$$\delta \Pi_N^{(el.)} = \delta \boldsymbol{\Lambda}^T \int_{s_a}^{s_b} \boldsymbol{\Phi} g \,\mathrm{d}s + \delta \boldsymbol{X}_1^T \int_{s_a}^{s_b} \mathbf{N}_1 \boldsymbol{n} \lambda \,\mathrm{d}s - \delta \boldsymbol{X}_2^T \int_{s_a}^{s_b} \mathbf{N}_2 \boldsymbol{n} \lambda \,\mathrm{d}s, \tag{45}$$

which differs from (24) only in the integration variable and domain, and from where we can recognise the residual vectors

$$\boldsymbol{R}_\lambda^{(el.)} = \int_{s_a}^{s_b} \boldsymbol{\Phi} g \,\mathrm{d}s, \qquad \boldsymbol{R}_1^{(el.)} = \int_{s_a}^{s_b} \mathbf{N}_1 \boldsymbol{n} \lambda \,\mathrm{d}s, \qquad \boldsymbol{R}_2^{(el.)} = -\int_{s_a}^{s_b} \mathbf{N}_2 \boldsymbol{n} \lambda \,\mathrm{d}s. \tag{46}$$

The linearised virtual work (44) similarly becomes

$$\begin{aligned}
\Delta(\delta \Pi_N^{(el.)}) = {} & \delta \boldsymbol{\Lambda}^T \int_{s_a}^{s_b} \boldsymbol{\Phi} \boldsymbol{n}^T \mathbf{N}_1^T \,\mathrm{d}s \Delta \boldsymbol{X}_1 - \delta \boldsymbol{\Lambda}^T \int_{s_a}^{s_b} \boldsymbol{\Phi} \boldsymbol{n}^T \mathbf{N}_2^T \,\mathrm{d}s \Delta \boldsymbol{X}_2 \\
& + \delta \boldsymbol{X}_1^T \int_{s_a}^{s_b} \mathbf{N}_1 \boldsymbol{n} \boldsymbol{\Phi}^T \,\mathrm{d}s \Delta \boldsymbol{\Lambda} - \delta \boldsymbol{X}_2^T \int_{s_a}^{s_b} \mathbf{N}_2 \boldsymbol{n} \boldsymbol{\Phi}^T \,\mathrm{d}s \Delta \boldsymbol{\Lambda} \\
& - \delta \boldsymbol{X}_1^T \int_{s_a}^{s_b} \lambda \left[\mathbf{N}_1 \mathbf{A} \mathbf{N}_1^T + \mathbf{N}_1 \mathbf{B} \mathbf{N}_1'^T + \mathbf{N}_1' \mathbf{B}^T \mathbf{N}_1^T + \mathbf{N}_1' \mathbf{C} \mathbf{N}_1'^T \right] \mathrm{d}s \Delta \boldsymbol{X}_1 \\
& + \delta \boldsymbol{X}_1^T \int_{s_a}^{s_b} \lambda \left[\mathbf{N}_1 \mathbf{A} \mathbf{N}_2^T - \mathbf{N}_1 \mathbf{B} \mathbf{N}_2'^T + \mathbf{N}_1' \mathbf{B}^T \mathbf{N}_2^T - \mathbf{N}_1' \mathbf{C} \mathbf{N}_2'^T \right] \mathrm{d}s \Delta \boldsymbol{X}_2 \\
& + \delta \boldsymbol{X}_2^T \int_{s_a}^{s_b} \lambda \left[\mathbf{N}_2 \mathbf{A} \mathbf{N}_1^T + \mathbf{N}_2 \mathbf{B} \mathbf{N}_1'^T - \mathbf{N}_2' \mathbf{B}^T \mathbf{N}_1^T - \mathbf{N}_2' \mathbf{C} \mathbf{N}_1'^T \right] \mathrm{d}s \Delta \boldsymbol{X}_1 \\
& - \delta \boldsymbol{X}_2^T \int_{s_a}^{s_b} \lambda \left[\mathbf{N}_2 \mathbf{A} \mathbf{N}_2^T - \mathbf{N}_2 \mathbf{B} \mathbf{N}_2'^T - \mathbf{N}_2' \mathbf{B}^T \mathbf{N}_2^T + \mathbf{N}_2' \mathbf{C} \mathbf{N}_2'^T \right] \mathrm{d}s \Delta \boldsymbol{X}_2,
\end{aligned} \tag{47}$$

from where the contact-element tangent stiffness matrices follow as

$$\begin{aligned}
\mathbf{K}_{\lambda 1}^{(el.)} &= \left(\mathbf{K}_{1\lambda}^{(el.)} \right)^T = \int_{s_a}^{s_b} \boldsymbol{\Phi} \boldsymbol{n}^T \mathbf{N}_1^T \,\mathrm{d}s, \qquad \mathbf{K}_{\lambda 2}^{(el.)} = \left(\mathbf{K}_{2\lambda}^{(el.)} \right)^T = -\int_{s_a}^{s_b} \boldsymbol{\Phi} \boldsymbol{n}^T \mathbf{N}_2^T \,\mathrm{d}s, \\
\mathbf{K}_{11}^{(el.)} &= -\int_{s_a}^{s_b} \lambda \left[\mathbf{N}_1 \mathbf{A} \mathbf{N}_1^T + \mathbf{N}_1 \mathbf{B} \mathbf{N}_1'^T + \mathbf{N}_1' \mathbf{B}^T \mathbf{N}_1^T + \mathbf{N}_1' \mathbf{C} \mathbf{N}_1'^T \right] \mathrm{d}s, \\
\mathbf{K}_{12}^{(el.)} &= \int_{s_a}^{s_b} \lambda \left[\mathbf{N}_1 \mathbf{A} \mathbf{N}_2^T - \mathbf{N}_1 \mathbf{B} \mathbf{N}_2'^T + \mathbf{N}_1' \mathbf{B}^T \mathbf{N}_2^T - \mathbf{N}_1' \mathbf{C} \mathbf{N}_2'^T \right] \mathrm{d}s, \\
\mathbf{K}_{21}^{(el.)} &= \int_{s_a}^{s_b} \lambda \left[\mathbf{N}_2 \mathbf{A} \mathbf{N}_1^T + \mathbf{N}_2 \mathbf{B} \mathbf{N}_1'^T - \mathbf{N}_2' \mathbf{B}^T \mathbf{N}_1^T - \mathbf{N}_2' \mathbf{C} \mathbf{N}_1'^T \right] \mathrm{d}s, \\
\mathbf{K}_{22}^{(el.)} &= -\int_{s_a}^{s_b} \lambda \left[\mathbf{N}_2 \mathbf{A} \mathbf{N}_2^T - \mathbf{N}_2 \mathbf{B} \mathbf{N}_2'^T - \mathbf{N}_2' \mathbf{B}^T \mathbf{N}_2^T + \mathbf{N}_2' \mathbf{C} \mathbf{N}_2'^T \right] \mathrm{d}s.
\end{aligned} \tag{48}$$

Penalty method

The penalty method can be introduced very similarly to the mortar method, see (29), (30) and (31). The unbiased contact-element residuals (46) eventually become

$$\boldsymbol{R}_1^{(el.)} = \int_{s_a}^{s_b} \mathbf{N}_1 \boldsymbol{n} \lambda \,\mathrm{d}s, \qquad \boldsymbol{R}_2^{(el.)} = -\int_{s_a}^{s_b} \mathbf{N}_2 \boldsymbol{n} \lambda \,\mathrm{d}s. \tag{49}$$

and its tangent stiffness matrices (48) become

$$\begin{aligned}
\mathbf{K}_{11}^{(el.)} &= -\int_{s_a}^{s_b} \lambda \left[\mathbf{N}_1 \mathbf{A} \mathbf{N}_1^T + \mathbf{N}_1 \mathbf{B} \mathbf{N}_1'^T + \mathbf{N}_1' \mathbf{B}^T \mathbf{N}_1^T + \mathbf{N}_1' \mathbf{C} \mathbf{N}_1'^T \right] - \varepsilon \mathbf{N}_1 \boldsymbol{n} \boldsymbol{n}^T \mathbf{N}_1^T \,\mathrm{d}s, \\
\mathbf{K}_{12}^{(el.)} &= \int_{s_a}^{s_b} \lambda \left[\mathbf{N}_1 \mathbf{A} \mathbf{N}_2^T - \mathbf{N}_1 \mathbf{B} \mathbf{N}_2'^T + \mathbf{N}_1' \mathbf{B}^T \mathbf{N}_2^T - \mathbf{N}_1' \mathbf{C} \mathbf{N}_2'^T \right] - \varepsilon \mathbf{N}_1 \boldsymbol{n} \boldsymbol{n}^T \mathbf{N}_2^T \,\mathrm{d}s, \\
\mathbf{K}_{21}^{(el.)} &= \int_{s_a}^{s_b} \lambda \left[\mathbf{N}_2 \mathbf{A} \mathbf{N}_1^T + \mathbf{N}_2 \mathbf{B} \mathbf{N}_1'^T - \mathbf{N}_2' \mathbf{B}^T \mathbf{N}_1^T - \mathbf{N}_2' \mathbf{C} \mathbf{N}_1'^T \right] - \varepsilon \mathbf{N}_2 \boldsymbol{n} \boldsymbol{n}^T \mathbf{N}_1^T \,\mathrm{d}s, \\
\mathbf{K}_{22}^{(el.)} &= -\int_{s_a}^{s_b} \lambda \left[\mathbf{N}_2 \mathbf{A} \mathbf{N}_2^T - \mathbf{N}_2 \mathbf{B} \mathbf{N}_2'^T - \mathbf{N}_2' \mathbf{B}^T \mathbf{N}_2^T + \mathbf{N}_2' \mathbf{C} \mathbf{N}_2'^T \right] - \varepsilon \mathbf{N}_2 \boldsymbol{n} \boldsymbol{n}^T \mathbf{N}_2^T \,\mathrm{d}s.
\end{aligned} \tag{50}$$

3.5. Active set strategy

Active set strategy is used to determine which nodes participate in the contact. The unbiased formulation uses the algorithm summarised in Tomec and Jelenić (2022) for the mortar method. For the activation of nodes, residual vectors $\boldsymbol{R}_\lambda$ from (26) (mortar) and (46) (unbiased) are used as they conveniently correspond to the weighted gap. The activation criteria then reads

$$\sum_{\substack{(el.) \text{ if} \\ (n) \in (el.)}} R_\lambda^{(n,el.)} < 0, \tag{51}$$

where (n) denotes a particular node. Once the node is activated, the residual starts to contribute to the global solution and goes to zero as the iterative procedure converges. For deactivation, the value of the Lagrange multiplier at a node is checked. If it is positive (representing an attractive force), the node is deactivated.

The solution algorithm is the same as in Tomec and Jelenić (2022) and uses an inner loop for finding the static equilibrium with the active set frozen and the outer *contact loop* which updates the activation of nodes and repeats the equilibrium search. A contact step refers to a single cycle of the contact loop. At the end of the contact step, the nodes that are deactivated are examined to see if they meet the activation criterion, while the nodes that are activate are turned off based on the deactivation criterion. More advanced algorithms such as (Alart and Curnier, 1991) exist, however, for the sake of clarity of presentation we leave them for future research.

4. Numerical examples

This section puts the presented formulations to test to assess their properties and compare them. In all examples geometrically-exact beam elements developed by Simo and Vu-Quoc (Simo and Vu-Quoc, 1986)

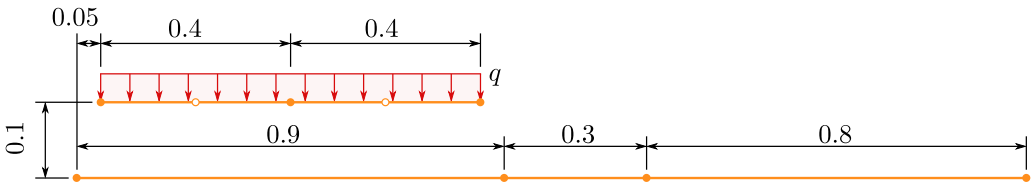

Fig. 4. Patch test: setup.

Table 1
Abbreviations for contact elements.

Abbreviation	Method
M2	mortar method with two nodes per element,
M1	mortar method with a single node per element,
MP	mortar method with penalty method,
U1	unbiased line-to-line method a single node per element,
UP	unbiased line-to-line method with penalty method.

Table 2
Patch test: Norm of gap evaluated at integration points after sliding.

Method	M2	M1	U1
gap	3.88×10^{-18}	3.47×10^{-18}	2.78×10^{-16}

are used. Abbreviations for different contact elements are summarised in Table 1. Both formulations are designed for arbitrary order of interpolation of Lagrange multiplier field.

4.1. Patch test

A patch test is conducted first to test the unbiased line-to-line method's ability to compute the exact gap value and to handle activation of nodes due to sliding. A beam consisting of two elements is positioned above a rigid surface simulated by a three first-order-element beam with fixed degrees of freedom. The problem geometry is given in Fig. 4. Both beams have a circular cross-section with radius $\rho = 0.005$ and material properties $E = 210 \times 10^9$ and $\nu = 0.3$. An external uniformly distributed loading $q = 1$ is applied to the top beam along the entire length of the beam. In the first load step, an equilibrium in contact is sought, while the next 100 steps consist of pushing the top beam horizontally along the bottom beam by a step $\Delta x = 0.01$. The tolerance is set to 10^{-12} for the energy norm.

We know from Tomec and Jelenić (2022) and Bosten et al. (2022) that the mortar method passes the patch test with almost zero gap. For the unbiased method with a single Lagrange-multiplier node per element, the results are similar. Using 4 integration points per element, the norm of all values of gap function evaluated in these points is close to zero as summarised in Table 2. With these results we can confirm that the method passes the patch test for zero-order interpolation. For higher-order interpolations of the Lagrange-multiplier field, the Newton–Raphson method experiences instabilities during sliding and consequently diverges. It is a consequence of discontinuous Lagrange multiplier interpolation which results in poorly conditioned tangent stiffness matrix. It also hints to shortcomings in the algorithm for determination of the integration boundaries, where the main complexity lies in handling the variety of possible special cases due to numerical imprecision. The unbiased line-to-line method therefore best works in combination with a constant Lagrange-multiplier interpolation.

4.2. Contact objectivity test

The following test has been designed to test objectivity of a line-to-line contact formulation with respect to beam numbering. Two horizontal cantilever beams are placed in parallel one above the other at the distance $2\rho = 0.006$ between. A vertical point force is applied to the top beam at its free end to bend it towards the bottom beam. Both beams are made of the same material with parameters $EA = 13351$, $GA_1 = 4982$, $GA_2 = 4982$, $GI_t = 0.0623$, $EI_1 = 0.08345$, $EI_2 = 0.08345$ and with a circular cross-section with radius $\rho = 0.003$. Both beams are of initial length $L = 0.05$ and discretised using two first-order geometrically exact beam elements. Four integration points are used for each contact element. The load is gradually increased in 7 quasi-static steps to the final magnitude of 42.

Table 3
Contact objectivity test: Displacements of the free end of the top beam.

	M1		U1	
	$x_{\text{top end}}$	$z_{\text{top end}}$	$x_{\text{top end}}$	$z_{\text{top end}}$
A	0.02281696	−0.00766457	0.02293061	−0.0073395
B	0.02292918	−0.00736453	0.02293061	−0.0073395
B-A	0.00011222	0.00030005	3.469×10^{-18}	4.337×10^{-18}

This test is conducted using the mortar and the unbiased line-to-line formulation twice (runs A and B), with the contact sides toggled in the two runs. Displacements of the top beam's free end are given in Table 3. Comparison of the displacements after changing the sides in the contact algorithm confirms that the new formulation is free from bias, unlike the mortar method which shows a certain amount of discrepancies. Deformation of the entire setup is illustrated in Fig. 5.

4.3. Cantilever test

This test is similar to Example 2 from Tomec and Jelenić (2022) and Example 4.2 from Bosten et al. (2022) and simulates a beam to rigid body contact. This example also has an analytical solution derived by Bosten et al. in Bosten et al. (2023). A cantilever beam is placed above another beam with all the degrees of freedom fixed, simulating a rigid body. Both beams have material parameters: $EA = 6.28 \times 10^6$, $GA = 0.242 \times 10^6$, $GJ_t = 0.12$ and $EI = 0.16$. Radius of the circular cross-section is 0.001. The top beam is discretised using 8 quadratic elements while the bottom beam consists of a single linear element. A distributed force $q = 10$ is applied to the top beam in 30 equal load steps. Geometry of the setup is given in Fig. 6. All contact elements use 4 integration points.

Fig. 7 shows the final deformed state obtained by the unbiased line-to-line method with a single Lagrange multiplier per element. The aspect ratio of the figure is such that the deformations are clearly visible. Figs. 8(a) and 8(b) show the final contact pressure in the tested formulations. Qualitatively the contact pressure agrees with the benchmark solution presented in Bosten et al. (2023). Elements sharing the contact-force model (the same Lagrange-multiplier interpolation order or the same penalty parameter) produce closely related results. This is also observed for the convergence rate in Fig. 8(c), which shows the penalty parameter for which the contact is successfully evaluated.

According to Tomec and Jelenić (2022), higher interpolation orders in the mortar method provides better fulfilment of the contact condition with higher oscillations in the contact pressure. It is interesting to see in Fig. 8(a), that even a single-node interpolation results in some oscillations. The oscillations in the contact pressure strongly resemble the spectral leakage phenomenon well known in the signal processing community which is the result of a mismatch between the actual

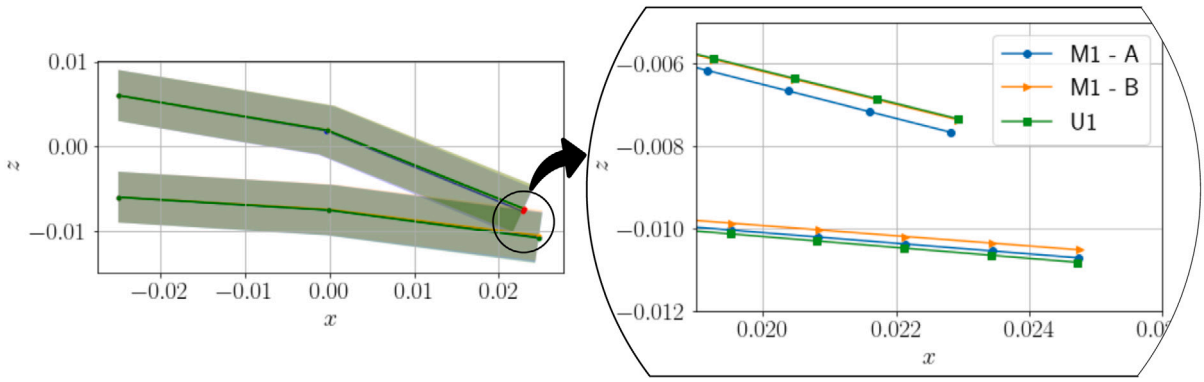

Fig. 5. Final deformed state of the dual-beam system computed using the mortar and the unbiased formulation.

Table 4
Cantilever test: Formulation performance comparison.

	M2	M1	MP ($\epsilon_0 = 10^5$)	U1	UP ($\epsilon_0 = 10^5$)
total number of iterations	154	82	81	82	81
mean number of iterations per contact step	2.23	2.19	2.70	2.10	2.70
relative computation time (reference: M2)	1.00	0.52	0.40	0.87	0.73

frequency of the signal and the discrete frequencies of the Fourier transform (Carlson and Crilly, 2009). The same reasoning can be applied here. The discontinuity in the pressure cannot be described exactly so it spreads to the neighbouring nodes within the contact region (the contact constraints do not permit the leakage to be distributed on both sides of the discontinuity). This happens because of the integration over the boundaries of the contact as the integration zone is not precisely computed. The penalty method (MP and UP) for lower penalty parameters on the other hand experiences a smooth transition as the contact conditions are strongly enforced. This is at the expense of a larger penetration at the contact boundary. When the penalty parameter is increased, similar oscillations appear — see Fig. 9. Again, the discontinuity cannot be modelled exactly while, at the same time, the gap function cannot compensate with large enough penetration due to the increased stiffness, which manifests in the form of the oscillations.

Higher interpolation order means more discontinuities in the system due to the activation of Lagrange-multiplier degrees of freedom, which is reflected in a larger number of contact steps even though the convergence in a particular contact step is similar (observe total number of iterations vs. mean number of iterations per contact step in Table 4).

Table 4 shows the total number of iterations and normalised computation time for all the formulations, for the same number of integration points, tolerances, step-sizes and all other input parameters. For this example, the mortar element with the penalty method is the fastest, being 23% faster than its Lagrange-multiplier counterpart, while the unbiased method is consistently slower than the mortar method (83% difference between MP and UP and 67% M1 and U1). Since there are no large deflections in the test, the contact elements are all defined at the beginning and there is no need for contact search algorithm. The test, therefore, only measures the performance of the computation of projections and convergence. Since this test is easy to converge (approximately 2 iterations per load step), the difference in convergence rate is not dominant in the total computation time. Using the penalty method reduces the computational time although it increases the total number of iterations. This indicates an inferior convergence path. The total number of iterations strongly depends on the selected penalty parameter as can be seen in Fig. 8(c).

4.4. Coupled bending

To analyse the contact algorithm stability under finite deformations, the following test utilises two deformable cantilever beams which are

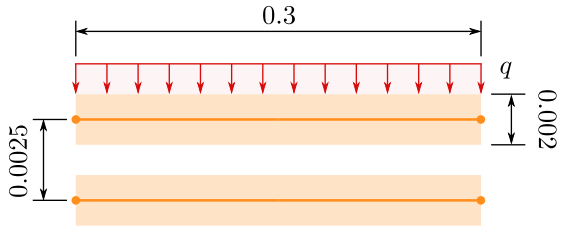

Fig. 6. Cantilever test: setup.

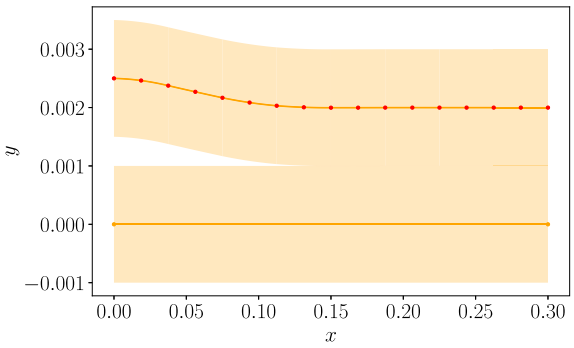

Fig. 7. Cantilever test: deformed state.

vertically aligned, see Fig. 10. The beams are pressed together by a constant pressure $q = 1000$ defined in the material frame. In the second load step, a bending moment $M = 1$ is applied to the free end of the bottom beam so that both beams are bent upwards. Beams have the same material parameters as in Section 4.3, while the penalty parameter is set to 10^7 where applicable. Different discretisations of both beams and contact are tested, with n denoting the number of beam elements on each beam.

Since first order beam elements result in a curve made of straight segments, the contact pressure is dominated by the geometrical constraints imposed by the interpolation. As this is a numerically difficult test case due to high compression loads, only second order beam elements are tested.

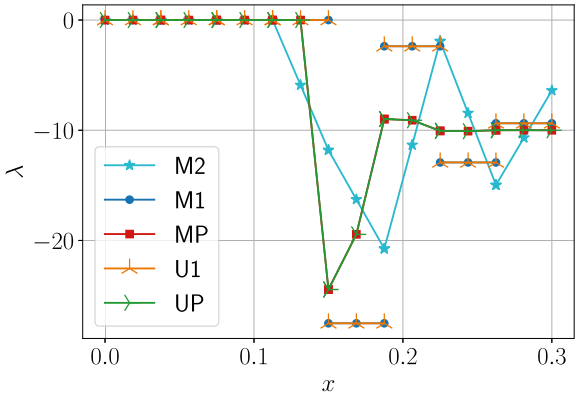

(a) Contact pressure using 8 elements per beam, $\varepsilon_0 = 10^7$

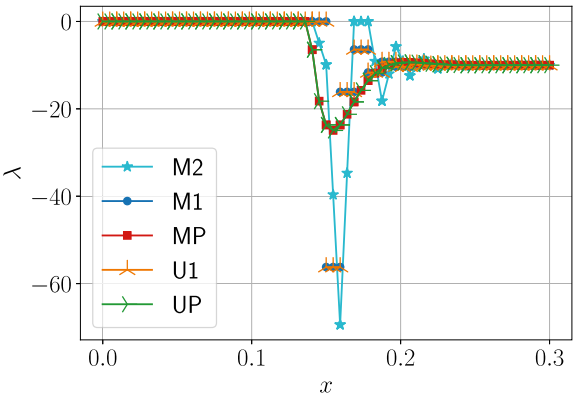

(b) Contact pressure using 32 elements per beam, $\varepsilon_0 = 10^7$

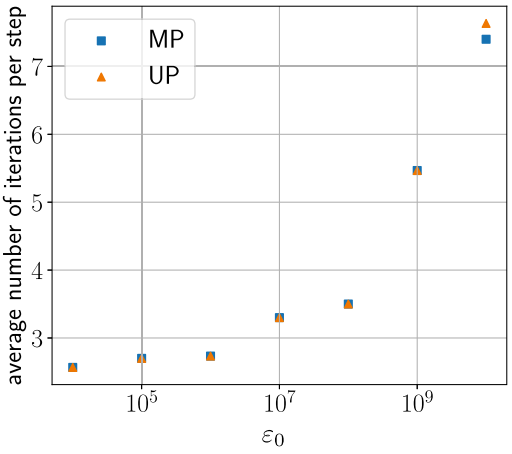

(c) Convergence with respect to the penalty parameter

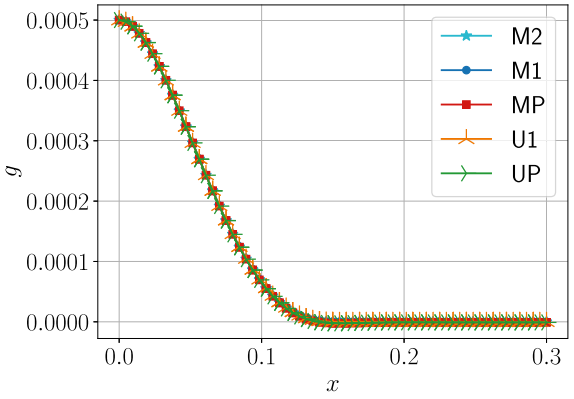

(d) Gap function using 32 elements per beam

Fig. 8. Cantilever test: convergence of Lagrange multipliers with refinement of beam mesh.

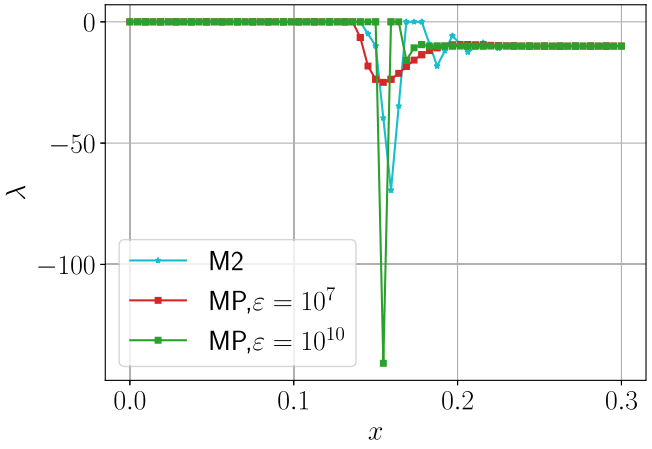

Fig. 9. Cantilever test: Contact pressure using 32 elements per beam; comparison of M2 and MP using two different penalty parameters.

Due to high bending deformation and axial stiffness, the top beam in the deformed configuration extends beyond the free end of the bottom beam (see Fig. 11). The high bending stiffness also induces some separation just before the tip. This effect is captured by all contact discretisations tested here and results in a pressure spike on

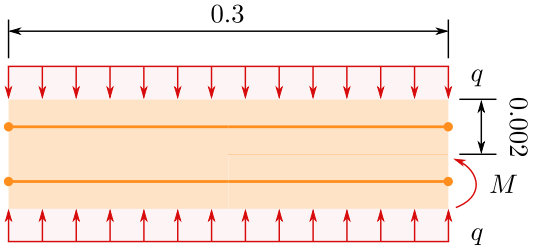

Fig. 10. Coupled bending: setup.

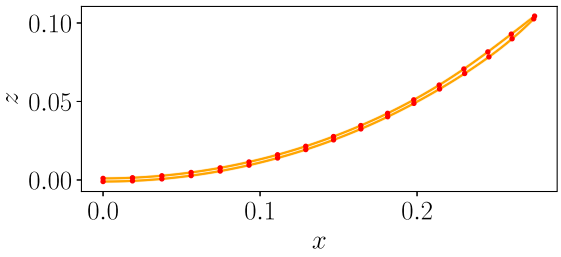

Fig. 11. Coupled bending: deformed state computed with 16 elements per beam.

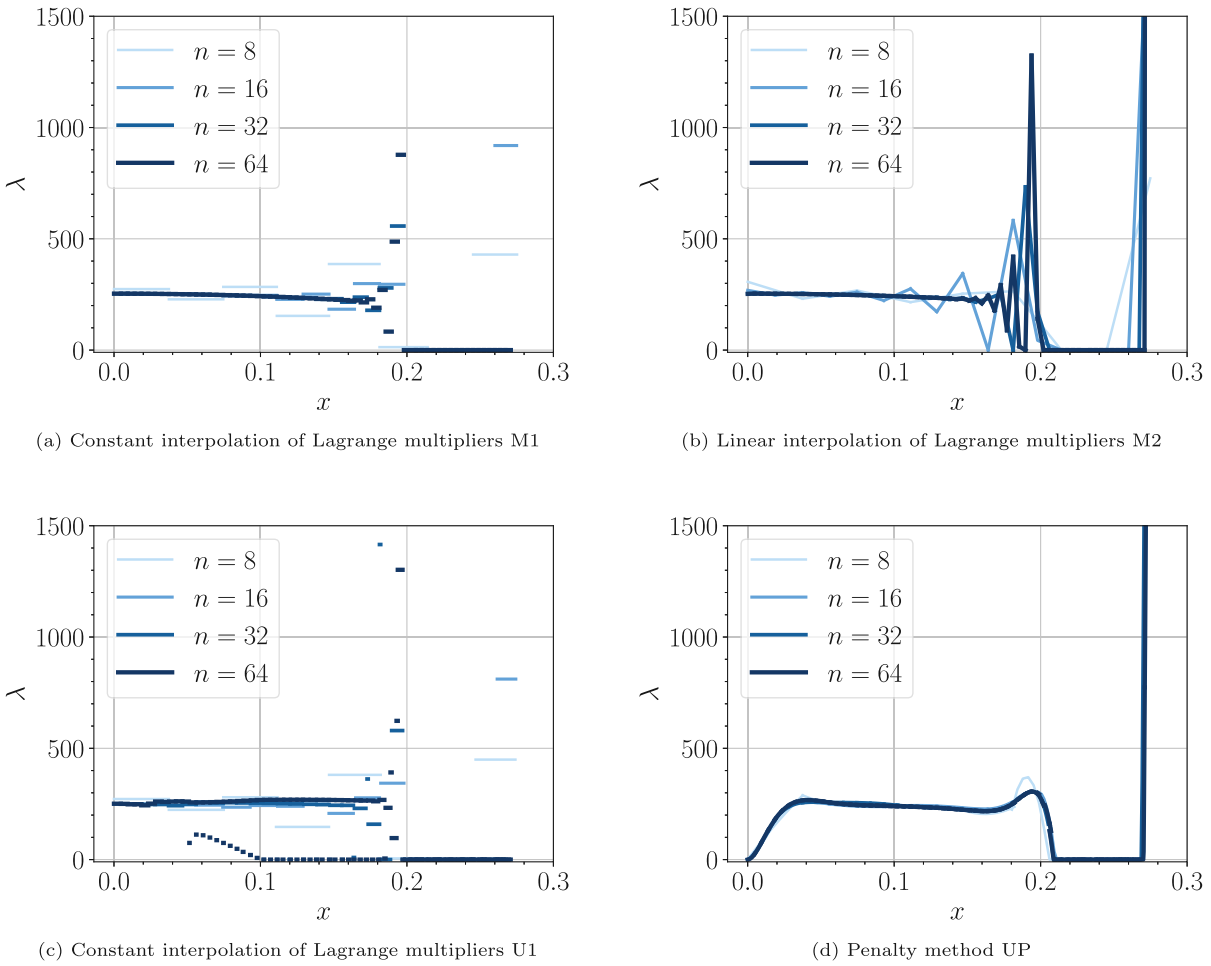

(a) Constant interpolation of Lagrange multipliers M1

(b) Linear interpolation of Lagrange multipliers M2

(c) Constant interpolation of Lagrange multipliers U1

(d) Penalty method UP

Fig. 12. Coupled bending: convergence of Lagrange multipliers with refinement of beam mesh.

the tip, Fig. 12. A drop in the contact pressure is visible in the area just before that as the top beam deforms away from the bottom one. The separation causes oscillations in the contact pressure where the numerical procedure integrates over a discrete jump.

Using the U1 method, one can observe similar results as with M1, but there are also some short contact elements which do not contribute to the contact, even though they are well within the contact zone. This can be contributed to overconstraining as the larger neighbouring elements do the heavy lifting. This short elements are a product of the segment-based integration and can cause potential instabilities as is shown in example 4.5.

This oscillation between two constant values is called the checkerboard mode (Cheng and Ye, 2002) and can be potentially triggered by the piecewise constant interpolation in any mortar formulation, which is in our case methods U1 and M1. To stabilise it, one can penalise the pressure difference in adjacent contact elements (Puso et al., 2012).

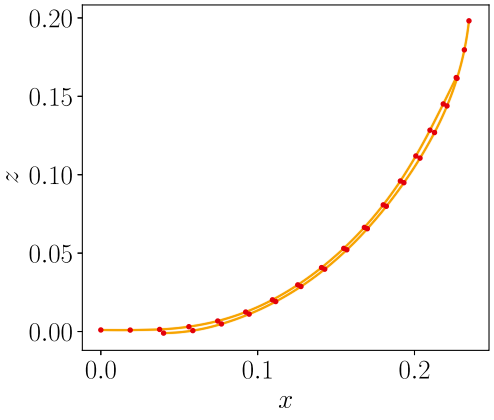

Fig. 13. Coupled bending with sliding: deformed state computed with 16 elements per beam.

4.5. Coupled bending with sliding

This is a continuation of example 4.4 and tests the contact method during sliding with high deformation. After the bending, the bottom beam is displaced at its support in the direction of the x axis for a displacement u. The displacement is applied in increments of 0.0002. As the two beams separate their combined bending stiffness decreases and the deformation of both beams increases even further. The final deformed shape at $u = 0.04$ is shown in Fig. 13.

The evolution of contact during sliding is shown in Fig. 15. From the plots we can see, that the contact zone continuously evolves. The contact zone is shortening while also a new pressure jump appears at the beginning of the contact zone. This results in high oscillations for the mortar method, Fig. 14, especially with higher number of elements. Nevertheless, the mortar method is stable and can solve the sliding problem without difficulties.

In contrast, the algorithm U1 experiences convergence problems during sliding. Since U1 uses segment-based integration as discussed in Section 3.4: Discretisation, this approach produces more degrees of freedom than mortar method which results in poorer conditioning

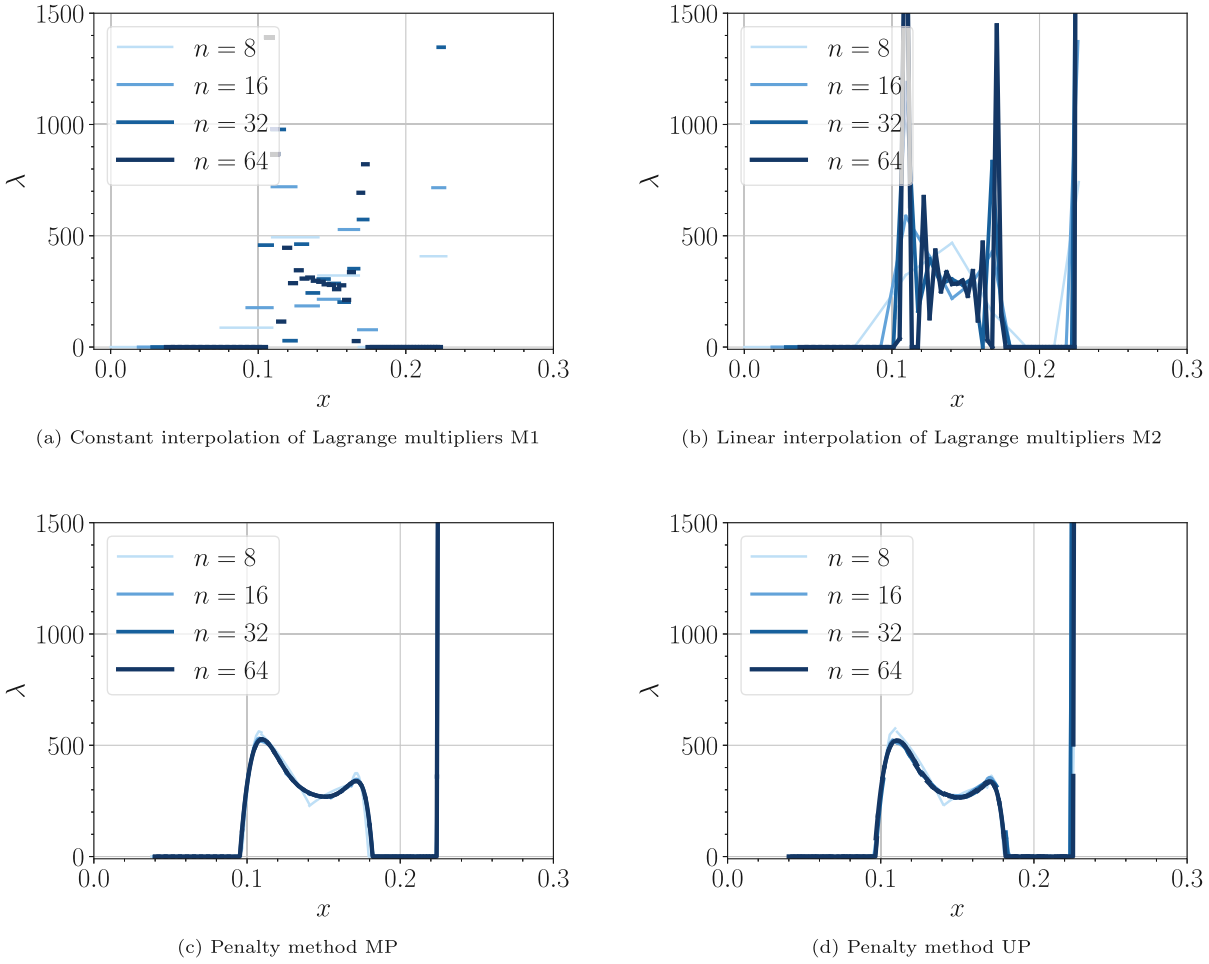

(a) Constant interpolation of Lagrange multipliers M1

(b) Linear interpolation of Lagrange multipliers M2

(c) Penalty method MP

(d) Penalty method UP

Fig. 14. Coupled bending with sliding: Convergence of Lagrange multipliers with refinement of beam mesh.

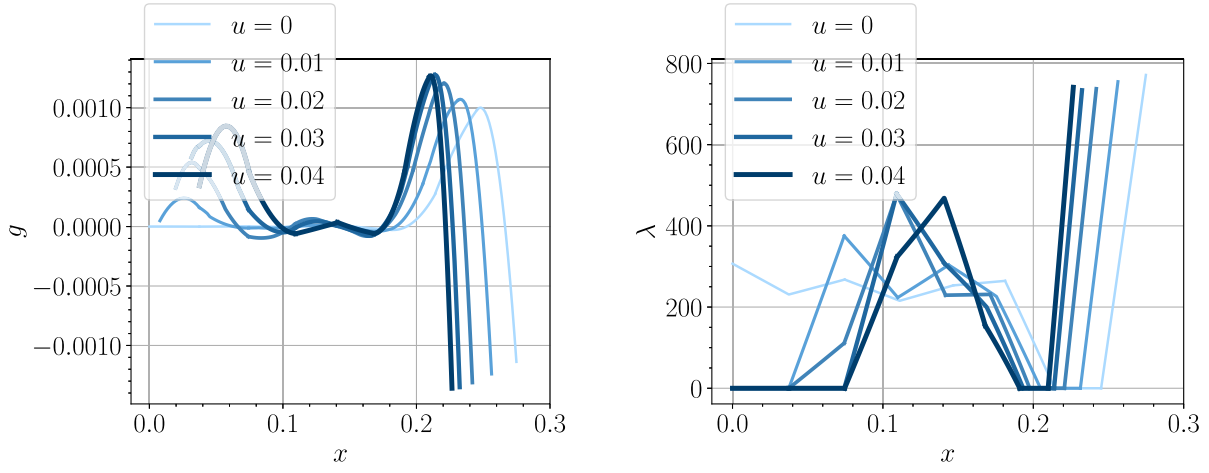

Fig. 15. Coupled bending with sliding: evolution of the contact with sliding computed with M2 and 8 beam elements.

of the numerical system and introduces more nonlinearities during sliding as the elements are created and destroyed. Interestingly, the penalty variant does not share the difficulties in this regard as it is not burdened with determining the active set of Lagrange multipliers, etc.

The penalty method again shows that the discontinuities present no problem and one obtains a continuous contact pressure. This is true for both MP and UP algorithms. As shown in the previous example in Fig. 8(c), the convergence highly depends on the penalty parameter which prevents higher values which would result in lower penetration.

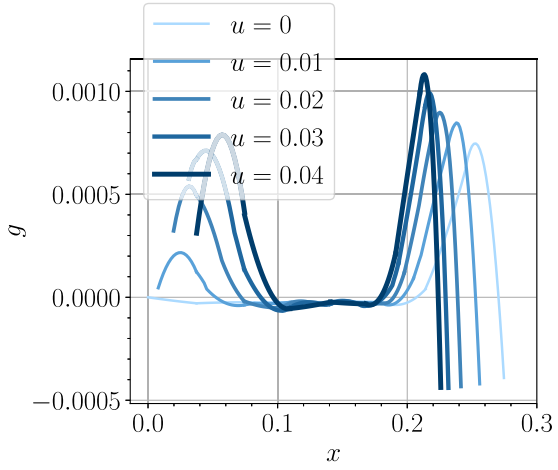

Fig. 16. Coupled bending with sliding: evolution of the contact with sliding computed with MP and 8 beam elements.

Fig. 16 shows the evolution of the gap function at different points of the simulation for the penalty formulation MP. Comparing it to the results obtained with M2 in Fig. 15, the maximum penetration is similar, however, the penetration is present throughout the contact zone as is expected for the penalty formulation, as the contact force requires penetration to exist. The average penetration is closer to zero with the M2 method as it allows some positive gap in the middle.

4.6. Twisting beams

Two parallel cantilever beams are placed one above the other and separated by an initial gap of 0.0005. The beams are of length 1 and material parameters $EA = 0.628$, $GA = 0.242$, $GJ_t = 0.12$ and $EI = 0.16$. The cross-section is circular with radius 0.001. The beams are fixed at one end, while the other is displaced in a circular fashion to complete a full revolution in 40 load steps. The nodes on the displaced end of the beams are allowed to freely rotate. Each beam is discretised using 16 quadratic elements. The iterative process is stopped when the energy norm 10^{-8} is achieved.

Fig. 17 shows the deformed configuration of the beams. The results show some asymmetry due to different boundary conditions on each end as can be seen both in the gap and contact-force distribution in Figs. 18(a) and 18(b). Comparison of the mortar and the unbiased method with the same contact-force model shows complete matching of the results in all respects: gap distribution, contact-force distribution and the number of iterations (see Figs. 18(a), 18(b) and Table 5). The unbiased method is slower because each element is computationally more expensive while also more elements need to be evaluated.

As in Section 4.3, we can observe some oscillations in the contact pressure at the boundaries of the contact. The penalty method numerically introduces some finite stiffness of the cross-section resulting in smooth gap and pressure fields. This example confirms the results of the example 4.3. The total number of iterations is the same for the mortar and the unbiased method, while the computational efficiency remains in favour of the mortar method. The computational cost of the penalty method varies with the penalty parameter. For a low value, e.g. $\varepsilon_0 = 100$, the method is the fastest among the tested, while admittedly the results are physically questionable as the penetration is around 10% of the cross-section radius. For a larger value of the penalty parameter, e.g. $\varepsilon_0 = 400$, the computational cost increases as does the processing time, as visible in Table 5. The high number of iterations per step indicate that the load increment should be reduced for optimal performance. Dependency of the average number of iterations per step on the penalty parameter is plotted in Fig. 19. Interestingly, with 40 steps, the increase is not monotonous which we contribute to undetermined local anomalies. Since this is a large time-step increment for this example, its decrease is expected to smoothen the trend. This is supported by an additional data set at 48 time steps.

4.7. Braiding

This test is an extension of the Twisting beams test 4.6 and simulates a situation with more complicated contacts. Three fibres of diameter 0.0001 are simply supported on one end and have roller supports on the other to allow axial movement. Fibres are also unable to rotate around their axes by disabling rotational degree of freedom corresponding to the axial rotation in the simple support. The material properties of the fibres are: $EA = 250$, $GA = 90$, $GI_t = 50$ and $EI = 60$. Fibres are positioned in a vertical plane with 0.0001 gap between each of them, as shown in Fig. 20. Each fibre is 0.05 in length and is discretised using 25 beam elements.

Before starting the braiding motion, the fibres are tensed with an axial force of 10. Afterwards, the braiding process starts, which follows simple circular movement to switch the positions of the middle fibre end-point and the one of a side fibre, keeping an alternating pattern. The applied step size is $\pi/30$ requiring 60 steps to complete a full rotation of a fibre pair. The final deformed shape can be viewed in Fig. 21.

The results cannot be obtained with the mortar method using either constant or linear interpolation of the Lagrange-multiplier field — the system does not converge after the onset of contact. The mortar element with the penalty method MP is able to continue and complete about one rotation of a fibre pair. The unbiased formulation appears to be the best choice for this example with the penalty method element UP reaching 70 load steps and Lagrange-multiplier element U1 reaching almost two rotation as can be seen in Table 6. As this example represents the most general contact of the ones presented in this paper, this indicates that the mortar method might not always be the optimal formulation with respect to the robustness.

5. Conclusion

In this paper we have developed a new discretisation method for a distributed contact formulation. It is unbiased with respect to the selection of the contact sides. It results in two new contact finite elements for which we have provided residuals and full linearisation. We have shown that such approach can increase robustness, however, we have also noted that the designed algorithm is quite complex as it requires computation of integration boundaries. We have included also a derivation of the mortar method to illustrate the similarities between the two formulations.

The developed contact elements have been compared to each other in a set of examples with an emphasis on identifying objectivity, robustness and computational cost. We have highlighted several key findings:

Table 5
Twisting beams: Formulation performance comparison.

	M2	M1	MP $\varepsilon_0=100$	MP $\varepsilon_0=400$	U1	UP $\varepsilon_0=100$	UP $\varepsilon_0=400$
total num. of iter.	113	108	92	604	108	92	504
mean num. of iter. per contact step	2.05	2.0	2.3	15.1	2.0	2.3	12.6
rel. comp. time (ref.: M2)	1.00	1.16	0.64	4.2	1.39	0.95	5.2

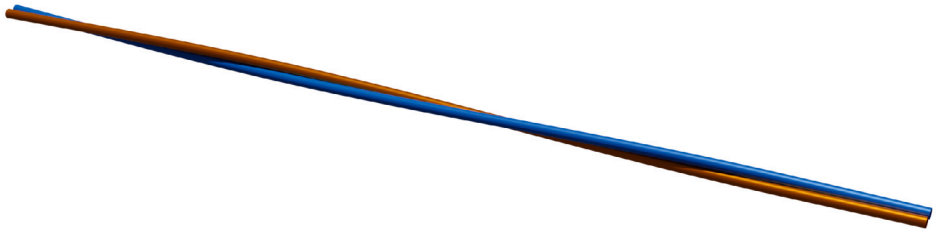

Fig. 17. Twisting beams: final deformed configuration after twisting (cross-section is scaled by a factor of 5 for visualisation purposes).

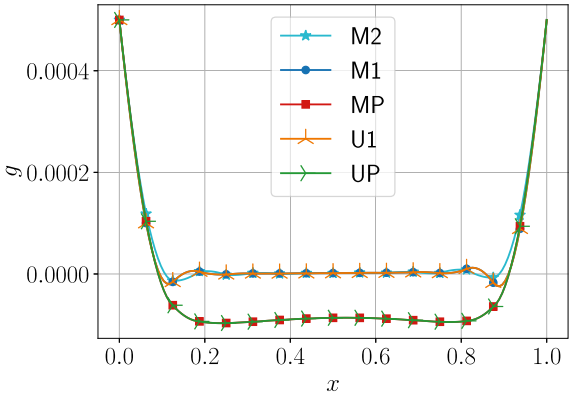

(a) Gap function, $\varepsilon_0 = 100$

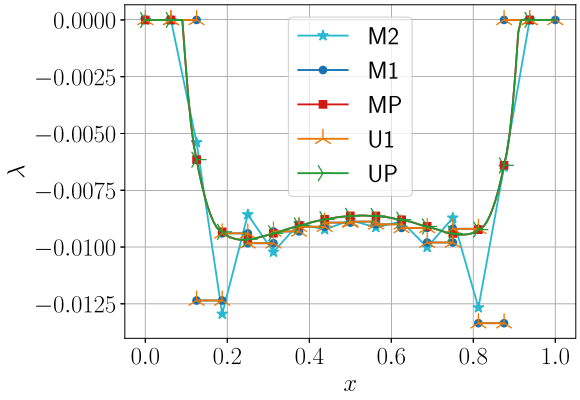

(b) contact pressure, $\varepsilon_0 = 100$

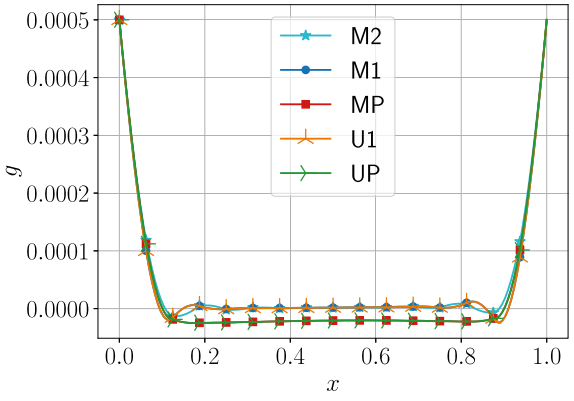

(c) Gap function, $\varepsilon_0 = 400$

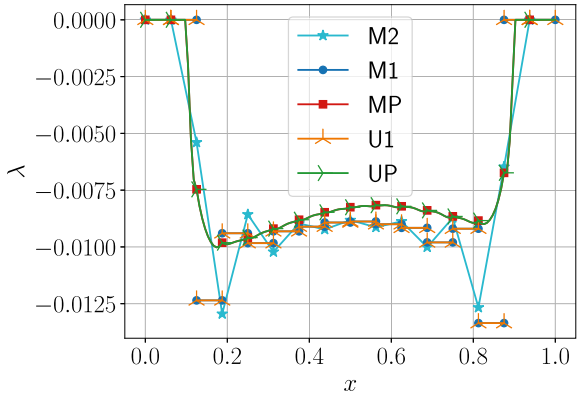

(d) contact pressure, $\varepsilon_0 = 400$

Fig. 18. Twisting beams: comparison of the final state of the contact.

Table 6
Braiding: Formulation performance comparison.

	M2	M1	MP ($\varepsilon_0 = 10^6$)	U1	UP ($\varepsilon_0 = 10^6$)
total number of load steps	17	17	61	111	70
mean number of iterations per contact step	/	/	2.78	2.33	2.20

- We have demonstrated the objectivity of the unbiased formulation.
- The Lagrange multipliers methods have been shown to exhibit superiority in terms of stability and robustness in most cases.
- From a computational standpoint, the penalty method offers faster performance.
- The mathematical model of a beam introduces discontinuities in the contact pressure, resulting in numerical fluctuations. These fluctuations tend to be more pronounced when higher-order interpolation of the Lagrange-multiplier field is used.
- In pursuit of stability, it is generally preferable to use a lower order of Lagrange-multiplier interpolation.
- Estimating the penalty parameter can be challenging, as it significantly impacts convergence and the final solution.
- The use of segment-based integration in combination with Lagrange multipliers method (method U1) can lead to instabilities during sliding.

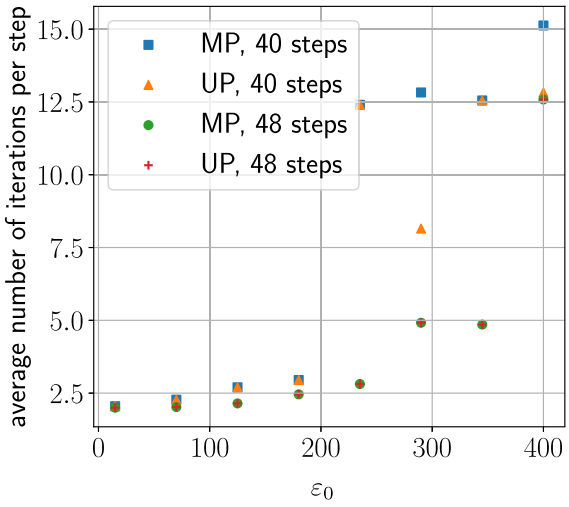

Fig. 19. Twisting beams: convergence with respect to the penalty parameter.

Fig. 20. Braiding: undeformed.

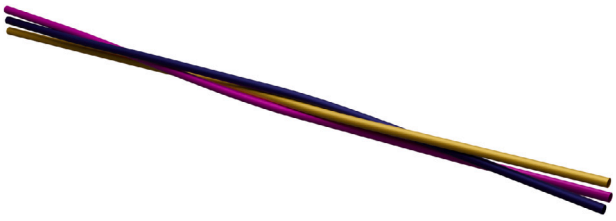

Fig. 21. Braiding: deformed.

Since the exact local behaviour in the contact region between beams is abandoned already by introducing geometrically exact beam theory (rigid cross-section), an important aspect of a beam-to-beam contact formulations is in the general robustness and reliability of the method. These, as we have shown through numerical experiments, may vary from case to case but tend to improve by using the Lagrange multipliers method and even further by making it unbiased.

Declaration of competing interest

The authors declare that they have no known competing financial interests or personal relationships that could have appeared to influence the work reported in this paper.

Data availability

Data will be made available on request.

Appendix. Unbiased projection algorithm

To obtain s_1 and s_2 from (34) and (35) we define

$$\boldsymbol{f}(s_1, s_2) = \begin{Bmatrix} (\boldsymbol{x}_1' + \boldsymbol{x}_2')^T (\boldsymbol{x}_1 - \boldsymbol{x}_2) \\ \frac{1}{2}(s_1 + s_2) - s \end{Bmatrix},$$

and look for the solution of the equation $\boldsymbol{f}(s_1, s_2) = \boldsymbol{0}$. The first-order Taylor series expansion then leads

$$\boldsymbol{f}\left(s_1 + h_1, s_2 + h_2\right) = \boldsymbol{f}(s_1, s_2) + \boldsymbol{\nabla}_{\{s_1, s_2\}} \boldsymbol{f}(s_1, s_2) \begin{Bmatrix} h_1 \\ h_2 \end{Bmatrix} = \boldsymbol{0}, \tag{A.1}$$

where

$$\boldsymbol{\nabla}_{\{s_1, s_2\}} \boldsymbol{f}(s_1, s_2) = \begin{bmatrix} \boldsymbol{p}^T \boldsymbol{x}_1'' + \boldsymbol{t}^T \boldsymbol{x}_1' & \boldsymbol{p}^T \boldsymbol{x}_2'' - \boldsymbol{t}^T \boldsymbol{x}_2' \\ \frac{1}{2} & \frac{1}{2} \end{bmatrix}.$$

Eq. (A.1) is then solved iteratively in the standard Newton–Raphson way.

References

Alart, P., Curnier, A., 1991. A mixed formulation for frictional contact problems prone to Newton like solution methods. Comput. Methods Appl. Mech. Engrg. 92 (3), 353–375. http://dx.doi.org/10.1016/0045-7825(91)90022-X.

Belgacem, F.B., 1999. The Mortar finite element method with Lagrange multipliers. Numer. Math. 84 (2), 173–197. http://dx.doi.org/10.1007/s002119900100.

Belgacem, F.B., Hild, P., Patrick, L., 1997. Approximation du problème de contact unilatéral par la méthode des éléments finis avec joints. C. R. Acad. Sci. - Series I - Mathematics 324 (1), 123–127. http://dx.doi.org/10.1016/s0764-4442(97)80115-2.

Bosten, A., Cosimo, A., Linn, J., Brüls, O., 2022. A mortar formulation for frictionless line-to-line beam contact. Multibody Syst. Dyn. 54 (1), 31–52. http://dx.doi.org/10.1007/s11044-021-09799-5.

Bosten, A., Denoël, V., Cosimo, A., Linn, J., Brüls, O., 2023. A beam contact benchmark with analytic solution. ZAMM - J. Appl. Math. Mech./Z. Angew. Math. Mech. http://dx.doi.org/10.1002/zamm.202200151.

Bottasso, C.L., Borri, M., 1998. Integrating finite rotations. Comput. Methods Appl. Mech. Engrg. 164 (3–4), 307–331. http://dx.doi.org/10.1016/S0045-7825(98)00031-0.

Carlson, A.B., Crilly, P.B., 2009. Communication Systems: An Introduction To Signals and Noise in Electrical Communication. McGraw-Hill Higher Education, p. 954.

Chamekh, M., Mani-Aouadi, S., Moakher, M., 2009. Modeling and numerical treatment of elastic rods with frictionless self-contact. Comput. Methods Appl. Mech. Engrg. 198 (47), 3751–3764. http://dx.doi.org/10.1016/j.cma.2009.08.005.

Cheng, X.-l., Ye, X., 2002. Analysis of the checkerboard mode and inf–sup condition. Commun. Numer. Methods. Eng. 18 (6), 451–458. http://dx.doi.org/10.1002/cnm.508.

Crisfield, M.A., Jelenić, G., 1999. Objectivity of strain measures in the geometrically exact three-dimensional beam theory and its finite-element implementation. Proc. R. Soc. A 455 (1983), 1125–1147. http://dx.doi.org/10.1098/rspa.1999.0352.

Durville, D., 2004. Modelling of contact-friction interactions in entangled fibrous materials. In: VI World Wide Congress on Computational Mechanics. Beijing.

Durville, D., 2010. Simulation of the mechanical behaviour of woven fabrics at the scale of fibers. Int. J. Mater. Form. 3 (SUPPL. 2), 1241–1251. http://dx.doi.org/10.1007/s12289-009-0674-7.

Durville, D., 2012. Contact-friction modeling within elastic beam assemblies: An application to knot tightening. Comput. Mech. 49 (6), 687–707. http://dx.doi.org/10.1007/s00466-012-0683-0.

Farah, P., Popp, A., Wall, W.A., 2015. Segment-based vs. element-based integration for mortar methods in computational contact mechanics. Comput. Mech. 55, 209–228. http://dx.doi.org/10.1007/s00466-014-1093-2.

Hante, S., Tumiotto, D., Arnold, M., 2022. A Lie group variational integration approach to the full discretization of a constrained geometrically exact Cosserat beam model. Multibody Syst. Dyn. 54 (1), 97–123. http://dx.doi.org/10.1007/s11044-021-09807-8.

Hüeber, S., Wohlmuth, B.I., 2005. A primal-dual active set strategy for non-linear multibody contact problems. Comput. Methods Appl. Mech. Engrg. 194 (27–29), 3147–3166. http://dx.doi.org/10.1016/j.cma.2004.08.006.

Ibrahimbegović, A., 1997. On the choice of finite rotation parameters. Comput. Methods Appl. Mech. Engrg. 149 (1–4), 49–71. http://dx.doi.org/10.1016/S0045-7825(97)00059-5.

Litewka, P., 2005. The penalty and lagrange multiplier methods in the frictional 3d beam-to-beam contact problem. Civ. Environ. Eng. Rep. 1 (1), 189–207.

Litewka, P., 2007. Hermite polynomial smoothing in beam-to-beam frictional contact. Comput. Mech. 40 (5), 815–826. http://dx.doi.org/10.1007/s00466-006-0143-9.

McDevitt, T.W., Laursen, T.A., 2000. A mortar-finite element formulation for frictional contact problems. Internat. J. Numer. Methods Engrg. 48 (10), 1525–1547. http://dx.doi.org/10.1002/1097-0207(20000810)48:10<1525::AID-NME953>3.0.CO;2-Y.

Meier, C., Popp, A., Wall, W.A., 2016. A finite element approach for the line-to-line contact interaction of thin beams with arbitrary orientation. Comput. Methods Appl. Mech. Engrg. 308, 377–413. http://dx.doi.org/10.1016/j.cma.2016.05.012.

Meier, C., Wall, W.A., Popp, A., 2017. A unified approach for beam-to-beam contact. Comput. Methods Appl. Mech. Engrg. 315, 972–1010. http://dx.doi.org/10.1016/j.cma.2016.11.028.

Popp, A., Gee, M., Wall, W., 2009. A finite deformation mortar contact formulation using a primal–dual active set strategy. Internat. J. Numer. Methods Engrg. 79, 1354–1391. http://dx.doi.org/10.1002/nme.2614.

Popp, A., Gitterle, M., Gee, M.W., Wall, W.A., 2010. A dual mortar approach for 3D finite deformation contact with consistent linearization. Internat. J. Numer. Methods Engrg. 83 (11), 1428–1465. http://dx.doi.org/10.1002/nme.2866.

Puso, M.A., 2004. A 3D mortar method for solid mechanics. Internat. J. Numer. Methods Engrg. 59 (3), 315–336. http://dx.doi.org/10.1002/nme.865.

Puso, M.A., Sanders, J., Settgast, R., Liu, B., 2012. An embedded mesh method in a multiple material ALE. Comput. Methods Appl. Mech. Engrg. 245–246, 273–289. http://dx.doi.org/10.1016/j.cma.2012.07.014.

Puso, M.A., Solberg, J.M., 2020. A dual pass mortar approach for unbiased constraints and self-contact. Comput. Methods Appl. Mech. Engrg. 367, 113092. http://dx.doi.org/10.1016/j.cma.2020.113092.

Simo, J.C., 1985. A finite strain beam formulation. The three-dimensional dynamic problem. Part I. Comput. Methods Appl. Mech. Engrg. 49 (1), 55–70. http://dx.doi.org/10.1016/0045-7825(85)90050-7.

Simo, J.C., Vu-Quoc, L., 1986. A three-dimensional finite-strain rod model. part II: Computational aspects. Comput. Methods Appl. Mech. Engrg. 58 (1), 79–116. http://dx.doi.org/10.1016/0045-7825(86)90079-4.

Sonneville, V., Brüls, O., Bauchau, O.A., 2017. Interpolation schemes for geometrically exact beams: A motion approach. Internat. J. Numer. Methods Engrg. 112 (9), 1129–1153. http://dx.doi.org/10.1002/nme.5548.

Sonneville, V., Cardona, A., Brüls, O., 2014. Geometrically exact beam finite element formulated on the special Euclidean group SE(3). Comput. Methods Appl. Mech. Engrg. 268, 451–474. http://dx.doi.org/10.1016/j.cma.2013.10.008.

Tomec, J., Jelenić, G., 2022. Analysis of static frictionless beam-to-beam contact using mortar method. Multibody Syst. Dyn. 55 (3), 293–322. http://dx.doi.org/10.1007/s11044-022-09823-2.

Wohlmuth, B.I., 2001. A mortar finite element method using dual spaces for the Lagrange multiplier. SIAM J. Numer. Anal. 38 (3), 989–1012. http://dx.doi.org/10.1137/S0036142999350929.

Wriggers, P., Simo, J.C., 1985. Note on tangent stiffness for fully nonlinear contact problems. Commun. Numer. Methods. Eng. 1 (5), 199–203. http://dx.doi.org/10.1002/cnm.1630010503.

Zupan, E., Zupan, D., 2019. On conservation of energy and kinematic compatibility in dynamics of nonlinear velocity-based three-dimensional beams. Nonlinear Dynam. 95 (2), 1379–1394. http://dx.doi.org/10.1007/s11071-018-4634-y.